Fig. 5. Cell-assembly activity during the wheel predicts behavioral errors during the maze. (**A**) Two example neurons from a session with seven left error trials (err). Correct trials are separated into left- and right-turn trials. (**B**) Normalized firing rates of 43 neurons simultaneously recorded during wheel running, ordered by the latency of peak firing rates during correct left trials (left). (Right) Firing sequence of the same neurons on correct right trials. (**C**) Firing sequence of neurons in a single error (left) trial. Neuronal order is the same as in (B). The firing sequence during the error trial is similar to that of the correct left trials. The correlation coefficient between correct and error trial sequences is 0.45 (fig. S13). (**D**) Percent of correctly predicted erroneous choices from the neuronal population activity.

firing patterns of neurons during wheel running (Fig. 5D). Altogether, these observations demonstrate that a particular sequence of neurons was activated in a reliable temporal order from the moment the rat entered the wheel to the time it reached the reward.

Because running speed, head position, and head direction during wheel running before left and right choices were apparently indistinguishable (fig. S1), the above findings indicate that trial differences in hippocampal assembly configurations cannot solely arise from instantaneous environmental inputs or the integration of motion signals.

Behavioral function of internally generated cell-assembly sequences. These findings demonstrate that the rat brain can generate continually changing assembly sequences. The patterns of the self-evolving neuronal assembly sequences depend on the initial conditions, and the particular sequences of cell assemblies are predictive of behavioral outcome.

Our results offer new insights into the relationship between hippocampal activity and navigation (2–7, 14–20, 30–33). Hippocampal firing patterns during maze navigation were similar to those during wheel running in the delayed alternation memory task with stationary environmental and body cues. Therefore, we suggest that hippocampal networks can produce sequential firing patterns in two possibly interacting ways: under the influence of environmental/idiot?hetic cues or by self-organized internal mechanisms. The high-dimensional and largely random (nontopographical) connectivity of the CA3 axonal system (35) and its inputs makes the hippocampus an ideal candidate for internal sequence generation (13, 33, 36, 37). The parameters of cell-assembly dynamics (including their trajectory and lifetimes) are probably affected by a number of factors, including experience-dependent and short-term synaptic plasticity (34, 38); asymmetric inhibition (39); brain state;

and, fundamentally, the character and context of the input. The evolving trajectory can be effectively perturbed, or updated, by external inputs in every theta cycle (40). Because of this flexibility in the sources of cell-assembly control, we hypothesize that neuronal algorithms, having evolved for the computation of distances, can also support the episodic recall of events and the planning of action sequences and goals (19). During learning, the temporal order of external events is instrumental in specifying and securing the appropriate neuronal representations, whereas during recall, imagination (35), or action planning, the sequence identity is determined by the intrinsic dynamics of the network.

References and Notes
1. J. O'Keefe, J. Dostrovsky, *Brain Res.* **34**, 171 (1971).
2. J. O'Keefe, L. Nadel, *The Hippocampus as a Cognitive Map* (Clarendon, Oxford, UK, 1978).
3. J. Huxter, N. Burgess, J. O'Keefe, *Nature* **425**, 828 (2003).
4. B. L. McNaughton, C. A. Barnes, J. O'Keefe, *Exp. Brain Res.* **52**, 41 (1983).
5. J. O'Keefe, N. Burgess, *Nature* **381**, 425 (1996).
6. R. U. Muller, J. L. Kubie, J. B. Ranck Jr., *J. Neurosci.* **7**, 1935 (1987).
7. B. L. McNaughton et al., *J. Exp. Biol.* **199**, 173 (1996).
8. D. O. Hebb, *The Organization of Behavior: A Neuropsychological Theory* (Wiley, New York, 1949).
9. E. Tulving, *Elements of Episodic Memory* (Clarendon, Oxford, UK, 1983).
10. L. R. Squire, *Psychol. Rev.* **99**, 195 (1992).
11. M. Abeles, *Corticotronics: Neural Circuits of the Cerebral Cortex*, (Cambridge Univ. Press, New York, 1991).
12. M. W. Howard, M. S. Fotedar, A. V. Datey, M. E. Hasselmo, *Psychol. Rev.* **112**, 75 (2005).
13. W. B. Levy, A. B. Hocking, X. Wu, *Neural Netw.* **18**, 1242 (2005).
14. L. M. Frank, E. N. Brown, M. Wilson, *Neuron* **27**, 169 (2000).
15. J. Ferbinteanu, M. L. Shapiro, *Neuron* **40**, 1227 (2003).
16. E. R. Wood, P. A. Dudchenko, R. J. Robitsek, H. Eichenbaum, *Neuron* **27**, 623 (2000).
17. J. A. Ainge, M. A. van der Meer, R. F. Langston, E. R. Wood, *Hippocampus* **17**, 988 (2007).
18. W. E. Skaggs, B. L. McNaughton, M. A. Wilson, C. A. Barnes, *Hippocampus* **6**, 149 (1996).
19. G. Dragoi, G. Buzsáki, *Neuron* **50**, 145 (2006).
20. J. R. Huxter, T. J. Senior, K. Allen, J. Csicsvari, *Nat. Neurosci.* **11**, 587 (2008).
21. G. Buzsáki, *Neuroscience* **31**, 551 (1989).
22. M. A. Wilson, B. L. McNaughton, *Science* **265**, 676 (1994).
23. K. Louie, M. A. Wilson, *Neuron* **29**, 145 (2001).
24. S. A. Deadwyler, T. Bunn, R. E. Hampson, *J. Neurosci.* **16**, 354 (1996).
25. H. Eichenbaum, P. Dudchenko, E. Wood, M. Shapiro, H. Tanila, *Neuron* **23**, 209 (1999).
26. A. Czurko, H. Hirase, J. Csicsvari, G. Buzsáki, *Eur. J. Neurosci.* **11**, 344 (1999).
27. H. Hirase, A. Czurko, J. Csicsvari, G. Buzsáki, *Eur. J. Neurosci.* **11**, 4373 (1999).
28. C. Geisler, D. Robbe, M. Zugaro, A. Sirota, G. Buzsáki, *Proc. Natl. Acad. Sci. U.S.A.* **104**, 8149 (2007).
29. K. M. Gothard, W. E. Skaggs, B. L. McNaughton, *J. Neurosci.* **16**, 8027 (1996).
30. J. O'Keefe, M. L. Recce, *Hippocampus* **3**, 317 (1993).
31. A. P. Maurer, S. L. Cowen, S. N. Burke, C. A. Barnes, B. L. McNaughton, *J. Neurosci.* **26**, 13485 (2006).
32. F. Sargolini et al., *Science* **312**, 758 (2006).
33. B. L. McNaughton, F. P. Battaglia, O. Jensen, E. I. Moser, M. B. Moser, *Nat. Rev. Neurosci.* **7**, 663 (2006).
34. S. Fujisawa, A. Amarasingham, M. T. Harrison, G. Buzsáki, *Nat. Neurosci.* **11**, 823 (2008).
35. X. G. Li, P. Somogyi, A. Ylinen, G. Buzsáki, *J. Comp. Neurol.* **339**, 181 (1994).
36. G. Kreiman, C. Koch, I. Fried, *Nature* **408**, 357 (2000).
37. J. E. Lisman, *Neuron* **22**, 233 (1999).
38. L. F. Abbott, W. G. Regehr, *Nature* **431**, 796 (2004).
39. M. Rabinovich, R. Huerta, G. Laurent, *Science* **321**, 48 (2008).
40. M. B. Zugaro, L. Monconduit, G. Buzsáki, *Nat. Neurosci.* **8**, 67 (2005).
41. We thank H. Hirase for sharing his data and C. Curto, C. Geisler, S. Ozen, S. Fujisawa, K. Mizuseki, A. Sirota, D. W. Sullivan, and R. L. Wright for comments. Supported by NIH (NS34994 and MH54671), NSF (SBE 0542013), the James S. McDonnell Foundation, NSF (A.A.), the Swartz Foundation (V.I.), and the Robert Leet and Clara Guthrie Patterson Trust (E.P.).

Experimental Test of Self-Shielding in Vacuum Ultraviolet Photodissociation of CO

Subrata Chakraborty,[1] Musahid Ahmed,[2] Teresa L. Jackson,[1] Mark H. Thiemens[1]*

Self-shielding of carbon monoxide (CO) within the nebular disk has been proposed as the source of isotopically anomalous oxygen in the solar reservoir and the source of meteoritic oxygen isotopic compositions. A series of CO photodissociation experiments at the Advanced Light Source show that vacuum ultraviolet (VUV) photodissociation of CO produces large wavelength-dependent isotopic fractionation. An anomalously enriched atomic oxygen reservoir can thus be generated through CO photodissociation without self-shielding. In the presence of optical self-shielding of VUV light, the fractionation associated with CO dissociation dominates over self-shielding. These results indicate the potential role of photochemistry in early solar system formation and may help in the understanding of oxygen isotopic variations in Genesis solar-wind samples.

Isotope-selective photodissociation, or self-shielding, is a process that occurs because of two major parameters: (i) dissociation by isotope-dependent spectral line absorption, and (ii) differential photolysis that depends on the isotopic abundances. As a result, when the spectral line corresponding to the major isotope ^{16}O saturates, the lines corresponding to the minor species (^{17}O, ^{18}O) do not, and equal dissociation of the minor species results with $\delta^{17}O = \delta^{18}O$. CO, the most abundant oxygen-bearing molecule in the nebula, satisfies these criteria, and self-shielding may occur, with equal dissociation rates of the minor isotopes. The consequence is preferential production of ^{17}O and ^{18}O atomic oxygen species in the region of the disk where self-shielding is effective. Such models assume that there is no other isotope ef-

fect associated with the photolysis, a hypothesis that has not been experimentally tested.

Isotopically selective photodissociation of CO is invoked as an important photochemical process in interstellar molecular clouds (1–3) to explain the observed abundance variation of minor isotopomers of CO ($^{13}C^{16}O$, $^{12}C^{18}O$, $^{12}C^{17}O$). CO self-shielding has been proposed to account for the observed meteoritic oxygen and nitrogen isotopic anomalies (4). Recently, this process was proposed to act in a very hot location near the proto-Sun [within 0.6 astronomical unit (AU)], and the heavy atomic oxygen (^{17}O and ^{18}O) was transported through the "X"-wind to the chondrule-forming zone, whereas calcium-aluminum–rich inclusions (CAIs, the first condensed solids) formed from the residual primordial nebular gas (5). To avoid the erasure of the anomaly by isotopic exchange (6), it was also suggested that the self-shielding occurred in a low-temperature prenebular molecular cloud (7).

Another model invoked a region at low temperatures (~50 K) at 30 AU from the proto-Sun and above the disk midplane as the probable location of CO self-shielding (8). Formation of water

[1]Department of Chemistry and Biochemistry, University of California, San Diego, La Jolla, CA 92093–0356, USA. [2]Chemical Sciences Division, Lawrence Berkeley National Laboratory, 1 Cyclotron Road, Berkeley, CA 94720, USA.

*To whom correspondence should be addressed. E-mail: mthiemens@ucsd.edu

Table 1. The data obtained for the 14 experimental runs (1 through 4 and 6 through 15) grouped in 6 different experimental configurations. The parameters used in the experiments are also displayed (see supporting online material for blank correction).

Run #	Column density (10^{17} mol/cm²)	Exposure time (min)	Amount before fluorination (μmol)	Amount after fluorination (μmol)	N₂ blank (%)	O₂ blank from fluorination (μmol)	Measured $\delta^{17}O$ (‰)	Measured $\delta^{18}O$ (‰)	Blank corrected $\delta^{17}O$ (‰)	Blank corrected $\delta^{18}O$ (‰)	Slope	Ln form: $\delta^{17}O$ (‰)	Ln form: $\delta^{18}O$ (‰)
				1. 107.61 nm (11.52 ± 0.25 eV) at room temperature (in order of increasing column density)									
14	6.39	190	0.09	0.27	20.7	0.12	904.9	498.8	2136.9	1155.3	1.49	1143.2	767.9
15	10.6	510	0.25	0.45	13.0	0.14	5167.7	2430.0	8086.0	3792.6	1.41	2206.7	1567.1
				2. 105.17 nm (11.79 ± 0.25 eV) at room temperature (in order of increasing column density)									
8	4.39	890	0.27	0.49	12.1	0.16	1147.1	686.2	1823.0	1081.2	1.42	1037.8	733.0
2	5.87	450	0.91	1.17	10.7	0.13	670.3	412.4	767.9	470.1	1.48	569.8	385.3
3	6.61	450	0.53	0.70	12.3	0.09	1177.9	700.2	1367.9	810.5	1.45	862.0	593.6
6	7.71	600	1.02	1.14	13.5	–	1809.7	1079.3	1809.7	1079.3	1.41	1033.1	732.1
7	11.9	860	0.57	0.64	27.4	–	2445.9	1407.0	2445.9	1407.0	1.41	1237.2	878.4
				3. 105.17 nm (11.79 ± 0.25 eV) at dry-ice temperature (−66 °C) (in order of increasing column density)									
4	6.09	450	0.34	0.65	20.2	0.18	2031.5	1424.0	3108.1	2170.9	1.22	1413.0	1154.0
9*	7.54	825	0.20	35.05	0.10	34.81	43.5	43.5	5613.9	3676.4	1.22	1889.2	1542.5
11	9.37	450	0.17	0.41	10.6	0.20	2908.4	1905.3	6257.6	4081.9	1.22	1982.0	1625.7
				4. 97.03 nm (12.78 ± 0.25 eV) at room temperature									
12	6.81	435	0.59	0.88	5.8	0.24	829.8	703.1	1161.2	978.7	1.12	805.4	717.2
				5. 94.12 nm (13.17 ± 0.25 eV) at room temperature (in order of increasing column density)									
1	3.93	290	1.46	1.54	9.9	–	159.7	258.8	159.7	258.8	0.64	148.1	230.2
10†	7.03	430	0.49	0.56	9.3	0.02	7.7	11.7	7.6	11.3	0.67	7.6	11.3
				6. 94.12 nm (13.17 ± 0.25 eV) at dry-ice temperature (−66 °C)									
13	6.81	435	0.67	0.72	23.9	–	542.9	873.7	446.1	718.6	0.69	459.6	662.1

*Air leaked through the oxygen sample tube after fluorination. Condensables are separated cryogenically and the noncondensables (N₂) are separated via gas chromatography. From the measured amount of separated N₂, the air O₂ amount was estimated and used for the blank correction with an air O₂ isotopic composition of 12.1 and 23.5‰ for $\delta^{17}O$ and $\delta^{18}O$, respectively. †For unknown reasons, the δ values were quite low compared to those of a similar experiment (#1), though the slope value ($\delta^{17}O/\delta^{18}O$) was the same.

ice with anomalous heavy isotopic composition from self-shielded CO dissociation can account for the hydrous minerals of the Allende meteorite (9). Two major assumptions were made: (i) The initial nebular oxygen isotopic composition was considered to be that of CAIs ($\delta^{17}O = \delta^{18}O = -40‰$), and (ii) no isotopic fractionation occurred during CO photodissociation other than via the opacity effect. We test this second assumption through experimental isotopic measurements in the relevant spectral region.

CO absorbs VUV photons at discrete spectral lines, and the excited (Rydberg) states are mostly predissociated through interaction with contin-uum states (2). Between 90 and 110 nm, there are numerous (~41) strong absorption bands. All bands are not equally effective for photodissociation of CO; the lines assigned to bands with the largest oscillator strength yield the predominant contri-bution to the rate of photodissociation (2, 10). The lines at 107.61, 94.12, 95.01, 97.03, and 94.01 nm are most effective at lower optical depth, and at higher optical depth (11) the lines at 95.01, 94.01, 96.89, and 92.58 nm are the most effective and con-tribute substantially to the dissociation rate. Un-der nebular conditions (in the presence of H_2, $H_2/CO \sim 10^4$), CO lines are removed from the absorption lines by H_2 and H and do not effec-tively contribute to dissociation (lines at 91.37, 91.73, 92.87, 93.00, 93.11, 93.17, 94.63, 96.44, 98.56, 100.26, and 106.31 nm are shielded by the absorption lines of H_2 and H). Apart from shielding by the H_2 and H lines, some lines of minor isotopomers (e.g., ^{13}CO, $C^{17}O$, and $C^{18}O$) are shielded by CO lines because they lie close to one another and, therefore, there would be no ap-preciable self-shielding at the lines at 91.57, 91.60, 92.28, 95.62, 97.03, 98.98, and 107.61 nm (11). Hence, the total photodissociation rate is a com-bination of absorptions associated with many different transitions (table S1).

We used a windowless flow chamber with three stages of differential pumping (fig. S1) at the chemical dynamic beamline (9.0.2) located at the Advanced Light Source (ALS), Lawrence Berkeley National Laboratory. Ultrahigh-purity CO was passed through the cylindrical reaction chamber and was exposed to VUV synchrotron photons (10^{16} photons/s) from the beamline to dis-sociate CO to C and O atoms along the line of CO flow. During the irradiation period, two stainless-steel spirals at the outlet of the reaction chamber were frozen in liquid nitrogen (LN_2) and collected the final product CO_2, formed by reaction of O atoms and bath gas CO. The CO_2 was converted to O_2 by means of the fluorination method (12), and the oxygen isotopic ratios were determined by isotope ratio mass spectrometry (see supporting online material for details).

We used four different wavelengths in our experiments—107.61, 105.17, 97.03, and 94.12 nm—to investigate the wavelength and upper elec-tronic excited state–dependent isotopic fractionation in photodissociation. At several wavelengths, we ran the experiment at dry-ice temperatures to evaluate possible temperature dependencies.

Experimental results, conditions, sample amounts (with corresponding blanks), and isotopic compo-sitions (measured and blank-corrected values) for each run are presented in Table 1. Raw data were corrected for fluorination blanks, determined through (measured amount) tank CO_2 fluorina-tion of known oxygen isotopic composition. The isotopic composition of initial CO ($\delta^{17}O = 25.5$ and $\delta^{18}O = 51‰$) was determined several times by conversion to CO_2 through electric discharge (disproportionation) of CO (complete conversion), followed by fluorination. The heavy isotopes of O in the product CO_2 were relatively enriched com-pared to initial CO in a mass-independent manner (Table 1). The extent of isotopic enrichment was typically a few thousands per mil, depending on experimental conditions (column density and ex-posure time). This extent of isotopic fractionation is large compared to other known physical or chemical processes.

The oxygen isotopic composition of CO_2 is shown in Fig. 1, a three-isotope plot in logarith-mic scale [to incorporate the nonlinearity in cross δ-plot for large δ values (13)]. The product CO_2 was enriched in heavy O isotopes in all cases compared to the initial CO composition, and the resultant isotopic compositions were wavelength

Fig. 1. Oxygen isotope compo-sition of product CO_2 in a three-isotope plot (in logarithmic form to incorporate the nonlinearity in cross δ-plots for large δ values) showing wavelength-dependent fractionation pattern during CO photodissociation. The RT photolysis products at 107.61 and 105.17 nm [where the upper electronic state is $E^1\Pi$ and associated with "accidental-predissociation" via the channel $C(^3P) + O(^3P)$] are extended over a linear line with a slope value of 1.38 (with an intercept of 37.5‰), whereas the products at $-66°C$ of 105.17 nm are fractionated more than the RT data and follow a relatively lower slope of 1.21 (with an in-tercept of 14.5‰). The compo-sition of the product of 94.12 nm [which represents a different higher-state ($^1\Pi$) occupancy during VUV absorption and adiabatically dissociates to form $C(^1D)$ and $O(^1D)$] at RT follows a trend line of 0.64. The product of the same wavelength at a lower temperature ($-66°C$) shows larger fractionation, as observed for 105.17 nm, but has a slope value similar to that at RT. The photolysis product at 97.03 nm [which occupies another electronic state, $C^1\Sigma$, and dissociates through $C(^1D) + O(^3P)$ channel] lies in between the results of 94.12 and 105.17 nm.
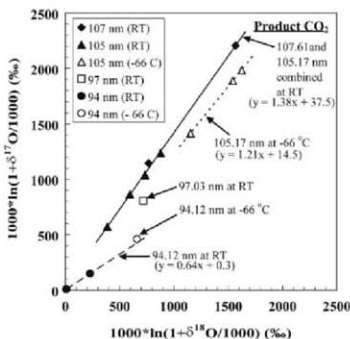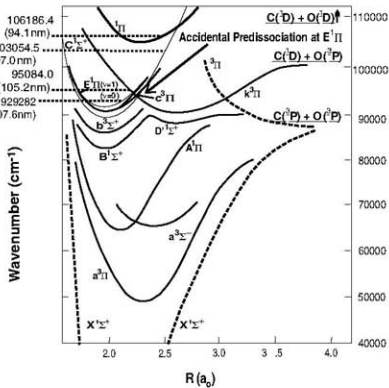

Fig. 2. Schematic dia-gram of the CO poten-tial energy curve, showing the specific upper-level occupations by different VUV photon absorption in this experiment. The upper–electronic state $E^1\Pi$ is associated with "acciden-tal predissociation," and its lower vibrational states are perturbed by another bound triplet state, $k^3\Pi$.

dependent. The range of isotopic composition at particular wavelengths derived from variation of column densities and exposure times. All fractionations, except for photolysis at 94.12 nm, were highly mass independent. The room temperature (RT) photolysis products at 107.61 and 105.17 nm extended over a linear line with a slope of 1.38 (with an intercept of 37‰), whereas the lower-temperature ($-66°C$) products at 105.17 nm were fractioned to a greater extent than were the RT products and follow a lower slope of 1.21 (with an intercept of 14.5‰). The compositions of the RT product at 94.12 nm define a trend line of 0.64 (with an intercept of 0.3‰). Results for the same wavelength at a lower temperature ($-66°C$) exhibit a larger fractionation, as observed for 105.17 nm, but define a similar slope value (single points lie over the RT trend line of 94.12 nm). The photolysis product at 97.03 nm (RT) is between the results of 105.17 and 94.12 nm.

Self-shielding occurs as a result of optical shielding of short UV light of the various isotopically substituted CO molecules and, hence, the fractionation is dependent on isotopic abundance and not mass. The models assume that no other isotopic fractionation is associated with photodissociation. CO self-shielding is possible through the band at 105.17 nm, but not through the band at 107.61 nm [2], because of line broadening. In contrast, our results show that the dissociation products for the bands at 105.17 and 107.61 nm follow an identical fractionation trend (slope value of 1.38). A similar result (e.g., no self-shielding) was anticipated for the line at 97.03 nm, where we observe a mass-independent fractionated photodissociation product. Self-shielding was predicted at the 94.12-nm line; however, the experimental data display no self-shielding effect. Hence, the different isotope effects during CO dissociation at different wavelengths can derive from the nature of higher electronic states and dissociation dynamics. In a schematic energy-level diagram compiled from [14–19] for CO (Fig. 2), the upper electronic state $E^1\Pi$ (a bound Rydberg state) is associated with a type of predissociation termed "accidental-predissociation" [20]. The lower rovibronic states of $E^1\Pi$ are perturbed by the presence of another triplet state, $k^3\Pi$ [21]. Predissociation from the $E^1\Pi$ state takes place via the bound Rydberg state $k^3\Pi$ state, assisted by a repulsive state to a near-resonance dissociative channel $C(^3P) + O(^3P)$. In this experiment, the vibrational energy states $v = 0$ and $v = 1$ of $E^1\Pi$ are populated by VUV photon absorption at 107.61 and 105.17 nm, respectively (Fig. 2), and lead to dissociation through the "accidental-predissociation" pathway, which proceeds via spin-orbit coupling between singlet and triplet states. Accidental predissociation is a well-known near-resonance effect that occurs for narrow ranges of rotational states (J states). Cacciani et al. [22, 23] showed that for $v = 0$ (107.62 nm), the higher J-value states are perturbed by the $k^3\Pi$ state, whereas lower J-value states are perturbed for the $v = 1$ (105.17 nm) state. The VUV source

used in our experiment is wide (full width at half maximum = 0.25 eV), and the two bands (105.17 and 107.62 nm) slightly overlap, but individually populate high rotational states (J states) at RT, which enhances the probability of accidental predissociation. Huge isotope effects have been observed previously as a result of near-resonance spin-orbit coupling between singlet-triplet states. Lim et al. [24] observed a large effect in Cl isotopes during a fluorescence study of OClO, and Bhattacharya et al. [25] observed a large isotope effect during CO_2 photodissociation and experimentally demonstrated that isotopic selective cross-over occurs between singlet and triplet surfaces due to spin-orbit coupling. A similar type of anomalous isotope-dependent predissociation in the $F^3\Pi_u$ ($v = 1$) state of O_2 has also been observed [26]. At 97.03 nm, the upper electronic state $^1\Sigma$ is populated via another singlet-triplet cross-over and dissociates through the $C(^1D) + O(^3P)$ channel. This singlet-triplet crossing is different from the one associated with the $E^1\Pi$ state and yields a different isotope selectivity. The dissociation at 94.12 nm is relatively straightforward: The $^1\Pi$ state is populated and adiabatically dissociates through the $C(^1D)$ and $O(^1D)$ channel [15]. Such dissociation usually yields a mass-dependent slope. The wavelength-dependent fractionation pattern (Fig. 1) emphasizes that the observed isotope effect is dominated by a physical-chemical dissociation mechanism of the CO molecule even in the presence of optical shielding of the light source. A mass-independent effect in CO_2 formation in the CO + O reaction (slope value close to unity) has been reported [27]. The observed nonzero intercepts of 37.5 and 14.5‰ (respectively for 107.61 and 105.17 nm combined at RT and for 105.17 nm at $-66°C$) as shown in Fig. 1 may be explained through this recombination effect as a secondary fractionation step and accounts for the nonzero intercept with the starting isotopic composition, as expected for a multistage fractionation process. The temperature dependence of fractionation is not yet clear, but may arise because the probability of a near-resonance singlet-triplet transition varies inversely with temperature, as was seen for vibrational energy transfer between isotopomers of CO at low temperatures [28].

A numerical analysis of absorption and dissociation cross sections of different VUV lines has quantified their differential share at the edge of a molecular cloud in the total absorption cross section (table S1). Van Dishoeck and Black [2] estimated that 58% of $C^{18}O$ dissociates through band 31 (105.17 nm) at the center of the cloud; however, this band contributes little to the absorption (1.0%) and dissociation (1.4%) at the edge of the cloud. Other lines used in our experiment—107.61, 97.03, and 94.12 nm—contribute appreciably to the absorption and dissociation. During the exposure of a nebular gas by solar VUV radiation, the lines listed in table S1 are all available for CO dissociation (assuming VUV photodissociation of CO at the outer edge of the disk).

The actual isotopic composition of atomic oxygen is double that of the CO_2 that we measured, because CO_2 was produced after reaction of an O atom with normal CO. Determination of the O-atom compositions due to self-shielding (calculated through photon absorption by different isotopologs of CO with a fixed set of parameters, e.g., initial photon flux, column density, and exposure time) for all experiments in Table 1 yields a fractionation trend line of slope 1 in a three-isotope oxygen plot (fig. S2). The column density used in our experiments was optically thicker (due to experimental constraint) than that thought to pertain in the solar nebula and may complicate the simple absorption calculation (fig. S2) due to pressure broadening. Nevertheless, a highly enriched anomalously fractionated O-atom reservoir is possible through photodissociation of CO at various wavelengths. Considering the low-temperature data (which are more fractionated and slightly depleted in ^{17}O compared to RT experiments), we conclude that CO dissociation at the cold regions of the solar nebula is a potential site for the generation of more O-atom reservoirs with high amounts of ^{17}O and ^{18}O relative to ^{16}O, but not via self-shielding.

Water plays a vital role in defining the oxygen isotopic distribution in the solar system as one-third of total oxygen resides in it [9, 29–32]. Recently, an extremely heavy oxygen isotopic composition ($\approx 180‰$ in $\delta^{17, 18}O$) of nebular water in aqueous altered meteoritic minerals has been reported [33]. Laboratory experiments have implied that oxygen isotope exchange between water in the gas phase and molten silicates at high temperatures can occur [34]. Cumulative evidence suggests that there was an anomalous oxygen isotopic reservoir. Our experiments are consistent with the formation of such a reservoir; however, they also indicate that self-shielding is not required, thus eliminating spatial dependencies. The results do not necessarily require the initial isotopic composition of the nebula to be $\delta^{18}O = \delta^{17}O = -40‰$, although this composition is not ruled out.

References and Notes

1. J. Bally, W. D. Langer, Astrophys. J. 255, 143 (1982).
2. E. F. van Dishoeck, J. H. Black, Astrophys. J. 334, 771 (1988).
3. S. R. Federman et al., Astrophys. J. 591, 986 (2003).
4. M. H. Thiemens, J. E. Heidenreich, Science 219, 1073 (1983).
5. R. N. Clayton, Nature 415, 860 (2002).
6. O. Navon, G. J. Wasserburg, Earth Planet. Sci. Lett. 73, 1 (1985).
7. H. Yurimoto, K. Kuramoto, Science 305, 1763 (2004).
8. J. R. Lyons, E. D. Young, Nature 435, 317 (2005).
9. R. N. Clayton, Annu. Rev. Earth Planet. Sci. 21, 115 (1993).
10. C. Letzelter, M. Eidelsberger, F. Rostas, J. Breton, B. Thieblemont, Chem. Phys. 114, 273 (1987).
11. S. Warin, J. J. Benayoun, Y. P. Viala, Astron. Astrophys. 308, 535 (1996).
12. S. K. Bhattacharya, M. H. Thiemens, Z. Naturforsch. A 44a, 435 (1989).
13. E. D. Young, G. Albert, H. Nagahara, Geochem. Cosmochim. Acta 66, 1095 (2002).
14. S. Wilson, Int. J. Quantum Chem. 12, 609 (1977).
15. D. L. Cooper, K. Kirby, J. Chem. Phys. 87, 424 (1987).
16. K. Kirby, D. L. Cooper, J. Chem. Phys. 90, 4895 (1989).

17. J. Baker *et al.*, *Chem. Phys.* **178**, 569 (1993).
18. A. Melinger, C. R. Vidal, *J. Chem. Phys.* **101**, 104 (1994).
19. J. Baker, F. Launay, *Chem. Phys. Lett.* **415**, 296 (2005).
20. J. D. Simmons, S. G. Tilford, *J. Mol. Spectrosc.* **49**, 167 (1974).
21. J. Baker, F. Launay, *J. Mol. Spectrosc.* **165**, 75 (1994).
22. P. Cacciani, W. Hogervorst, W. Ubachs, *J. Chem. Phys.* **102**, 8308 (1995).
23. P. Cacciani *et al.*, *Astrophys. J.* **499**, L223 (1998).
24. G. Lim, S. M. Lim, S. K. Kim, Y. S. Choi, *J. Chem. Phys.* **111**, 456 (1999).
25. S. K. Bhattacharya, J. Savarino, M. H. Thiemens, *Geophys. Res. Lett.* **27**, 1459 (2000).
26. B. R. Lewis, S. T. Gibson, J. P. England, G. Stark, J. B. West, *J. Chem. Phys.* **116**, 3286 (2002).
27. A. Pandey, S. K. Bhattacharya, *J. Chem. Phys.* **124**, 234301 (2006).
28. M. L. Turnidge, J. P. Reid, P. W. Barnes, C. J. S. M. Simpson, *J. Chem. Phys.* **108**, 485 (1998).
29. E. Anders, N. Grevesse, *Geochem. Cosmochim. Acta* **53**, 197 (1989).
30. B. Fegley Jr., *Space Sci. Rev.* **92**, 177 (2000).
31. E. D. Young, *Philos. Trans. R. Soc. Lond. A* **359**, 2095 (2001).
32. E. D. Young, *Earth Planet. Sci. Lett.* **262**, 468 (2007).
33. N. Sakamoto *et al.*, *Science* **317**, 231 (2007).
34. Y. Yu, R. H. Hewins, R. N. Clayton, T. K. Mayeda, *Geochem. Cosmochim. Acta* **59**, 2095 (1995).
35. This work was supported by NASA grant NNX07AJ81G under Origins and by the director, Office of Energy Research, Office of Basic Energy Sciences, Chemical Sciences Division of the U.S. Department of Energy under contract DE-AC02-05CH11231. Three reviewers are thanked for helpful suggestions that improved the manuscript.

Identification of Active Gold Nanoclusters on Iron Oxide Supports for CO Oxidation

Andrew A. Herzing,[1,2] Christopher J. Kiely,[1]* Albert F. Carley,[3] Philip Landon,[3] Graham J. Hutchings[3]*

Gold nanocrystals absorbed on metal oxides have exceptional properties in oxidation catalysis, including the oxidation of carbon monoxide at ambient temperatures, but the identification of the active catalytic gold species among the many present on real catalysts is challenging. We have used aberration-corrected scanning transmission electron microscopy to analyze several iron oxide–supported catalyst samples, ranging from those with little or no activity to others with high activities. High catalytic activity for carbon monoxide oxidation is correlated with the presence of bilayer clusters that are ~0.5 nanometer in diameter and contain only ~10 gold atoms. The activity of these bilayer clusters is consistent with that demonstrated previously with the use of model catalyst systems.

Gold nanoparticles on oxide supports are being used to catalyze an increasing number of reactions (*1–6*), but there is continuing interest in the relatively simple low-temperature oxidation of CO (*1–3, 7*), especially concerning the nature of the active species. Some proposals emphasize the size and morphology of the gold particle and its interface with the support (*1, 8*), whereas others postulate that metal oxidation state (*9, 10*) and support material can have strong effects (*1, 11*). Most of the fundamental insights into this reaction have come from well-defined model studies (*12–15*) in which specific structures are tailor-made (*14*). However, the difficulty lies in linking these informative model studies to those carried out on real catalysts, which are inherently more complex. Here, we report a microscopy study of an Au/FeOx catalyst and demonstrate that, among a number of gold nanostructures present, the origin of the activity is associated uniquely with gold bilayer nanoclusters that are ~0.5 nm in diameter and contain ~10 Au atoms.

Gold supported on FeOOH is a highly active catalyst for the low-temperature oxidation of CO (*16*), and we recently reported a link between catalyst performance and catalyst drying conditions (*10*). A pair of 2.9 atomic % Au/FeOx samples (denoted samples 1 and 2) were derived from the same coprecipitated precursor. Sample 1 was dried in a tube furnace (static air; furnace was ramped after insertion at 15°C/min to 120°C; 16 hours), whereas sample 2 was dried in a gas chromatography (GC) oven (flowing air; sample inserted into the furnace at 120°C; 16 hours). The Au loading in each was identical, and the underlying disordered FeOOH supports had similar surface areas (~190 $m^2 g^{-1}$). X-ray energy-dispersive spectroscopy (XEDS) analysis and high-angle annular dark-field (HAADF) imaging experiments (*10*) indicated that both samples contained 2- to 15-nm Au particles, with mean particle sizes of 5.4 nm for sample 1 and 7.0 nm for sample 2.

If the CO oxidation activity was dictated solely by the Au particle size, as some researchers have suggested (*1, 8*), then these two samples should have exhibited similar activities. In fact, sample 1 would probably be expected to have a slightly better performance by virtue of the Au particles being slightly smaller, on average. However, catalytic testing of these two samples under standard conditions (total flow rate of 66,000 h $^{-1}$; 0.5 volume % CO) revealed that sample 2 achieved 100% CO conversion at 25°C, whereas sample 1 gave only trace CO conversion (<1%). Even at much higher flow rates, sample 2 remained active (i.e., at a total flow rate of 450,000 vol.gas/vol.catalyst.h; the conversion was 25%), whereas sample 1 was totally inactive. Previously (*10*), we were unable to determine the origin of this marked effect because of the resolution and sensitivity limitations of the characterization techniques available. We consider that at least two possibilities exist to explain this difference: (i) There could be highly dispersed Au species present in sample 2 that were beyond the resolution limit of the conventional HAADF and
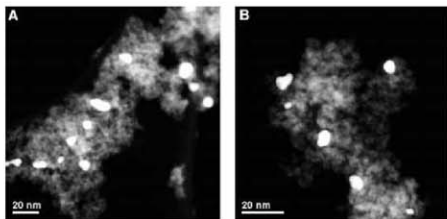

Fig. 1. Low-magnification aberration-corrected HAADF-STEM images from (**A**) the inactive, tube furnace catalyst (sample 1) and (**B**) the highly active, GC oven catalyst (sample 2). Au particle size distribution in both samples appears to be very similar at this magnification.

[1]Center for Advanced Materials and Nanotechnology, Lehigh University, 5 East Packer Avenue, Bethlehem, PA 18015–3195, USA. [2]National Institute of Standards and Technology, Surface and Microanalysis Science Division, 100 Bureau Drive, Mailstop 8371, Gaithersburg, MD 20899–8371, USA. [3]Cardiff Catalysis Institute School of Chemistry, Cardiff University, Cardiff, CF10 3AT, UK.

*To whom correspondence should be addressed. E-mail: chk5@lehigh.edu (C.J.K.); hutch@cardiff.ac.uk (G.J.H.)

scanning transmission electron microscopy (STEM)–XEDS techniques used previously, or (ii) the active catalyst contained some form of cationic Au species that was absent in the inactive sample. These two possibilities need not be mutually exclusive.

To investigate this unexpected difference in reactivity, we re-examined the samples using a state-of-the-art JEOL 2200FS in STEM mode equipped with a double-hexapole spherical aberration corrector manufactured by CEOS GmbH (17). The improvement to the HAADF image resolution, from the use of a 0.1-nm diameter aberration-corrected STEM probe containing 50 pA of current, makes this an ideal instrument to test whether there were Au species present in the highly active sample that were not detected earlier (10). Previously, this method has successfully been used to image atomic dispersions in the La/Al$_2$O$_3$, Pt/Al$_2$O$_3$, and Au/TiO$_2$ systems (18). The lower-magnification HAADF images for each of the dried Au/FeO$_x$ catalysts (Fig. 1, A and B) confirm the earlier results, with particles between 2 and 15 nm in diameter (Fig. 2, A to D, and figs. S1 and S2). However, at higher magnification (Fig. 2, A to D, and figs. S1 and S2), the actual Au particle size distribution and morphology in these samples are quite different. Both samples contain larger (2 to 15 nm) Au particles and a considerable number of individual Au atoms (indicated by white circles) dispersed on the iron oxide surface.

The observation of these individual atoms ensures that we are now resolving all of the types of Au species present. However, in addition a large population of subnanometer Au clusters was found in the active sample 2 (circled in black in Fig. 2, C and D) (see also fig. S1) that was not detected in the inactive sample. These Au clusters, the majority of which were 0.2 to 0.5 nm in diameter, contain at most only a few Au atoms. The contrast level exhibited by the 0.2- to 0.3-nm clusters, which are predominant in Fig. 2D, is similar to that of the individual Au atoms, implying that they are monolayer structures. In comparison, the 0.5-nm clusters highlighted in Fig. 2C exhibit markedly higher contrast in the HAADF image than that of the 0.2- to 0.3-nm clusters, suggesting that these larger clusters are most likely bilayers of Au.

Determination of the exact number of atoms in these various structures is complicated by several factors, including the slight contraction of the Au–Au bond distance known to occur in particles of this size (19). However, a rough estimate is still informative, and bilayers of ~0.5-nm lateral dimension would contain ~10 atoms (fig. S3A). In comparison, the 0.2- to 0.3-nm clusters of similar contrast to monolayers could contain about three to four atoms (fig. S3B). In contrast, an estimate based on the volumetric packing density of Au (~59 atoms/nm^3) suggests that the larger nanoparticles (5 to 7 nm) would contain 1900 to 5250 atoms if they have a hemispherical geometry. Thus, the subnanometer clusters and individual atoms observed in the highly active sample represent only a very minor fraction of the total Au content.

We used atomic-resolution STEM imaging to estimate the number fraction of the total Au particles represented by both clusters and nanoparticles by surveying several support areas that had ~100 larger nanoparticles, along with their neighboring vicinities (17). In terms of their frequency of observation, the individually adsorbed Au atoms represented 44 ± 4.5% of the Au species, whereas 19 ± 3.4% were 0.2- to 0.3-nm clusters, 18 ± 3.0% were 0.3- to 0.5-nm clusters, and 19 ± 3.5% were particles >1 nm (~50% were >5 nm).

However, considering the number of Au atoms in each of these structures (as discussed above) suggests that the individual atoms represent only 0.13 ± 0.07 atomic % and that the monolayer and bilayer subnanometer clusters combined represent only 1.05 ± 0.72 atomic % of the total Au loading (18), with the remaining 98.82 ± 0.80 atomic % of Au contained in the larger particles. Because of the very large disparity in the number of atoms they contain, the number of subnanometer clusters would have to exceed that of the 5-nm particles by a margin of nearly four to one for them to represent just 2 atomic % of the total Au loading. Therefore, it is probable that these minority Au species would not be easily detected with traditional "bulk" techniques such as extended x-ray absorption fine structure or Mossbauer spectroscopy, or even by surface analysis techniques such as x-ray photo-electron spectroscopy (XPS), because their contribution to the total signal would be minimal compared with that of the larger nanoparticles (17).

The statistical accuracy of the current HAADF analysis must be considered, because undercounting of the subnanometer Au clusters may result from the nature of the STEM imaging process in an aberration-corrected instrument. The ability to detect single atoms on an oxide is highly dependent on the vertical position of the focused electron probe relative to the surface (20). Because adsorbed atoms can be present on either the top or bottom surface of the underlying oxide particle, imaging with single-atom resolution is possible only when one of the surfaces is exactly in focus. Practically, this limitation means that in any given image, single atoms are probably only detected on one surface of the support particle, and atoms on the opposite side may not be visible, whereas larger nanoparticles can be detected on either side of the support over a much wider range of defocus values. In the intermediate case of 0.2- to 0.5-nm clusters, it is not clear if the same narrow defocus range required to resolve individual atoms is necessary. However, even if it is pessimistically assumed that our analysis has detected only 50% of the total number of all the individual Au atoms, the atomically dispersed Au would still represent only 61 ± 3.6% of the total number of
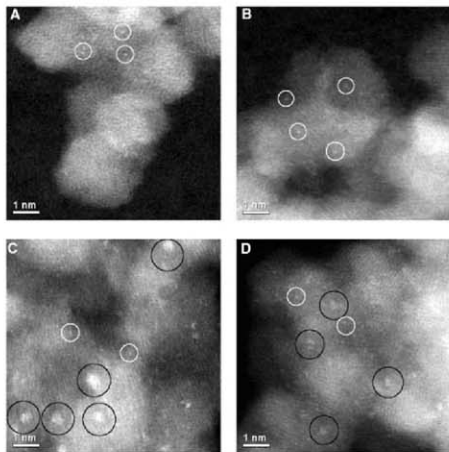

Fig. 2. High-magnification aberration-corrected STEM-HAADF images of (**A** and **B**) the inactive (sample 1) and (**C** and **D**) the active (sample 2) Au/FeO$_x$ catalysts acquired with the aberration-corrected JEOL 2200FS. The white circles indicate the presence of individual Au atoms, whereas the black circles indicate subnanometer Au clusters consisting of only a few atoms. Note the presence and image intensity difference of two distinct cluster-types: In (C) there are 0.5 nm higher-contrast clusters, whereas in (D) 0.2- to 0.3-nm low-contrast clusters dominate. This difference indicates that bilayer and monolayer subnanometer Au clusters are present in the active catalyst.

Au species, or ~0.25 ± 0.2 atomic % of the total Au loading.

The observation that the active species in our Au/FeO$_x$ catalysts consist of subnanometer clusters differs from numerous earlier investigations that identified 2- to 5-nm particles as the critical "nanostructure." However, a number of recent experimental and theoretical (21–23) studies have suggested that the CO oxidation activity should continue to increase as the Au particle size approaches 1 nm because of the presence of a larger fraction of Au atoms with low coordination in the smaller particles. Low-coordination Au atoms possess a d-band that is closer to the Fermi level than their close-packed counterparts, so they can adsorb O$_2$ molecules more readily. More specifically, Falsig et al. predicted that adsorption energies for CO and O are ideally suited for maximizing the reaction rate of CO oxidation at sixfold coordinated Au corner atoms, whereas the adsorption energies at close-packed Au faces are inferior for this purpose (23). Because clusters smaller than 1 nm should have an even greater fraction of low-coordinated Au atoms, reaching ~90% as a cluster size of 0.5 nm is approached, the role of subnanometer clusters may be crucial. Rashkeev et al. (24) have recently provided HAADF evidence that subnanometer mono-, bi-, and trilayer Au clusters coexisted in active Au/TiO$_2$ catalysts, although they were unable to isolate the relative importance of each of these subnanometer species and did not report any spectroscopic measurements to determine the possible role of substrate surface chemistry.

Scanning tunneling microscopy studies on model catalysts by Matthey et al. (15) showed that subtle changes in the chemistry of an oxide surface could alter the energetically favorable Au

structures that it stabilized and supported. Specifically, an oxygen-rich TiO$_2$ (110) surface could stabilize a range of Au species from one to seven atoms in size. In contrast, single Au atoms and Au trimers were the only stable configurations on a reduced TiO$_2$ (110) surface, whereas weakly bonded two-dimensional Au raftlike species were the only stable structures on a stoichiometric TiO$_2$ (110) surface. Similar oxygen-rich surfaces to those reported for TiO$_2$ have also been identified for FeO$_x$ (25); however, to our knowledge, systematic surface science studies and first-principle calculations of the stable Au structures present on FeOOH or Fe$_2$O$_3$ have not yet been performed.

On the basis of the observations of the two dried catalysts alone, we are unable to definitively comment on whether the bilayer 0.5-nm clusters, the monolayer 0.2- to 0.3-nm clusters, or both are responsible for the high activity observed or whether some subtle substrate chemistry effect is coming into play. Although individual Au atoms and larger (3 to 5 nm) particles are stable on both catalysts, the subnanometer Au clusters were only stable on the surface of catalyst 2 dried under a flowing air. The critical role played by such slight changes in the catalyst preparation route may help to explain the sometimes radically differing activities reported. We have used XPS to probe the nature of the surface species present in both samples. Analysis of the Au(4f) spectra (fig. S4.1) showed that, in both catalysts, the Au(4f$_{7/2}$) binding energy was 85.1 eV, characteristic of Au$^+$ species. The signal from sample 1 shows some broadening to higher binding energy that probably arose from a small amount of Au^{3+}, most likely present as AuOOH. The presence of hydroxylated Au species in this inactive sample suggests that the

lack of air circulation during the drying process inhibits the removal of the hydroxyl species from the catalyst surface, whereas this process occurs more efficiently under flowing air conditions.

This explanation was confirmed by the O(1s) and C(1s) spectra from these samples (figs. S4.2 and S4.3, respectively). Both catalysts exhibit a main O(1s) component characteristic of oxidic oxygen (O^2) at 530.4 eV, together with a shoulder at 531.8 eV. The latter feature originates from a combination of hydroxyl and carbonate species and is much more pronounced in sample 1. The C(1s) spectra, which show clear evidence of carbonate species, are similar for both. Therefore, the higher intensity of the O(1s) shoulder at 531.8 eV in the inactive catalyst 1 arises from the increased presence of hydroxyl groups relative to the active catalyst 2 dried in flowing air. This higher degree of hydroxylation and reduction of sample 1 seems to enhance the ability of the subnanometer clusters to sinter into larger particles and thus deactivate the catalyst. Hence, on the basis of the evidence presented so far, we are unable to determine whether it is the presence of subnanometer clusters or the differing degree of hydroxylation of the support that is controlling the activity.

Three separate portions of the highly active catalyst 2, denoted 3, 4, and 5, were calcined (3 hours at 400°, 550°, and 600°C, respectively). These heat treatments converted the support material to crystalline Fe$_2$O$_3$ and progressively reduced the surface area (catalysts 2: 190 m^2 g^{-1}, 3: 45 m^2 g^{-1}, 4: 16 m^2 g^{-1}, and 5: 11 m^2 g^{-1}). Atomic absorption spectroscopy confirmed that all of the Au (2.9 atomic %) was retained. CO conversion decreased from 100% in the fresh, uncalcined state to 91% (400°C), 31% (550°C), and <1% (600°C).

Fig. 3. Aberration-corrected STEM-HAADF images of the active 2.9 atomic % Au/FeO$_x$ catalyst 2 calcined for 3 hours at (**A** and **B**) 400°C (sample 3), (**C** and **D**) 550°C (sample 4), and (**E** and **F**) 600°C (sample 5). The heat-treatment procedures have substantially decreased the population of subnanometer Au clusters relative to the highly active, dried catalyst, while at the same time they have increased the population of particles in the 1- to 3-nm range.
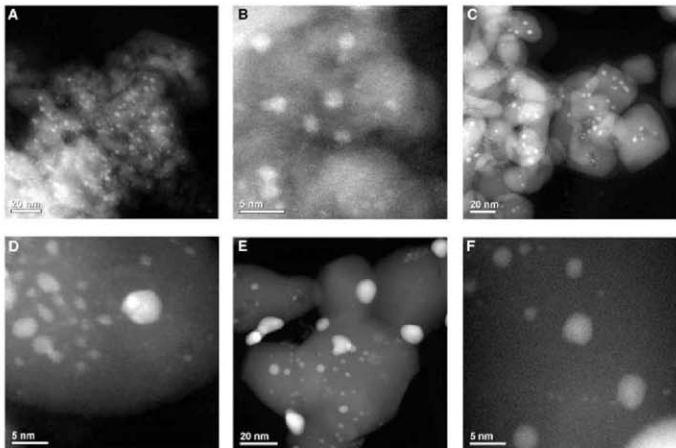
Aberration-corrected STEM-HAADF images (Fig. 3, A to F, and figs. S5.1 to 5.3) revealed that, although substantial particle sintering had occurred in all calcined catalysts, each sample also retained a population of the subnanometer clusters and individual Au atoms previously seen in the dried catalyst that had persisted through the various calcination treatments.

The number frequency of the various gold species encountered in samples 2, 3, 4, and 5 is summarized in Fig. 4. The number fraction of atomically dispersed species drops from ~44% to 35% across this sample set, whereas, simultaneously, the number fraction of particles greater than 1 nm progressively increases from 19 to 35%. However, our previous deductions from comparing samples 1 and 2 indicate that the supported subnanometer cluster species (and not the dispersed Au atoms or >1-nm particles) are active for CO conversion. It is also apparent from Fig. 4 that the number population of monolayer clusters remains relatively

constant at ~19%, whereas the bilayer cluster frequency gradually drops from 18% to <5% across this same sample set. Hence, the dramatic decrease in catalytic activity exhibited by samples 3, 4 and 5 can be directly correlated to the marked decrease in the number density of the 0.5-nm bilayer clusters as a result of their sintering into less active 1- to 2-nm Au particles.

XPS of samples 3, 4, and 5 (fig. S6) showed no notable difference in either of the Au(4f), Fe(3s), or Fe(2p) profiles (fig. S6.1 and 6.2) associated with this series of calcined catalysts. The O(1s) signals (fig. S6.3) are also all similar, with a high–binding energy tail indicating the presence of some residual hydroxyl and carbonate species, but these are very different from the dried sample (spectra shown in Fig. 5). The presence of carbonate species is confirmed by the weak, high binding energy feature in the C(1s) spectra (fig. S6.4). This feature is broader for sample 5, possibly reflecting carbonate species in distinct chemical envi-

ronments, and is consistent with small differences in the high–binding energy tail in the O(1s) spectrum for this sample.

To determine whether the small differences in samples 3 and 4 and the larger differences with the other samples correlate with the catalytic performance, we deconvoluted the O 1s signals into oxide and the higher–binding energy hydroxyl and carbonate species to obtain the relative fractions of each species present. However, the data for either the relative area percent of the higher–binding energy species (samples 2: 60%, 3: 28%, 4: 34%, and 5: 47%) or the hydroxyl/oxide ratio (samples 2: 1.5, 3: 0.4, 4: 0.5, and 5: 0.9) do not correlate with the observed activity trend. Thus, the similarity in the surface chemistry of samples 3 and 4, in particular, and the Au oxidation state in these calcined samples strongly imply that the progressive decrease in catalytic activity upon sintering is attributable to the gradual decrease in the population of the subnanometer bilayer clusters of gold.

Theoretical and model studies (23, 26–29) have shown that a critical factor in the catalytic activity of Au is the ability of the clusters to simultaneously adsorb both reactant molecules. Yoon et al. and Hakkinen et al. (27, 28) showed that the smallest Au cluster on MgO known to be active for CO oxidation is an octamer. Our observations are consistent with these theoretical studies, because the active bilayer subnanometer clusters in our system contain ~10 atoms, whereas the monolayer clusters (which have only three to four atoms) and the isolated Au atoms appear to be essentially inactive for CO oxidation.

Finally, CO oxidation activity of model Au catalysts on TiO_2 surfaces is maximized when the Au structures are two atomic layers thick (14, 28, 29), resulting in turnover frequencies (TOFs) as high as $3.7 \ s^{-1}$. In the present case, the TOF of catalyst 2 exhibiting 100% CO conversion was initially calculated to be $0.016 \ s^{-1}$ under standard conditions and $0.027 \ s^{-1}$ at the higher flow rate where total conversion (which is a more reliable estimate of the catalyst activity) was not observed. However, if the TOF is recalculated assuming that the bilayer clusters are the only active species and using a reasonable estimate of the fraction of the total Au that they contain (0.6 atomic %), the result is a TOF of $2.7 \ s^{-1}$ at the standard conditions and $3.5 \ s^{-1}$ at the higher–flow rate condition. These re-estimated TOF values are reasonably similar to the value of $3.7 \ s^{-1}$ of the model Au/TiO_2 catalyst (14).

These studies describe the full range of active and inactive Au species that are present within supported Au/FeO_x and Au/Fe_2O_3 catalysts. Subtle changes in sample-preparation route and calcination temperature can influence the formation, stability, and relative population of these various Au species. Herein, we have reported that highly active subnanometer Au clusters can be synthesized with a traditional chemical preparation route. Although the highest-activity catalysts correspond to uncalcined materials, experiments involving systematic calcination treatments have allowed us to
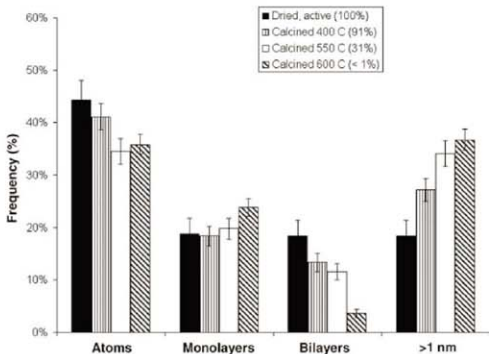

Fig. 4. Relative populations of (i) dispersed Au atoms, (ii) 0.2- to 0.3-nm monolayer Au clusters, (iii) 0.5-nm bilayer Au clusters, and (iv) Au nanoparticles >1 nm in diameter, as a function of catalyst calcination temperature and measured CO conversion. The error bars correspond to two SDs on the size measurements.

Fig. 5. O(1s) photoemission spectra from the Au/Fe_2O_3 catalysts (**A**) dried at 120°C and then calcined at (**B**) 400°C, (**C**) 550°C, and (**D**) 600°C.
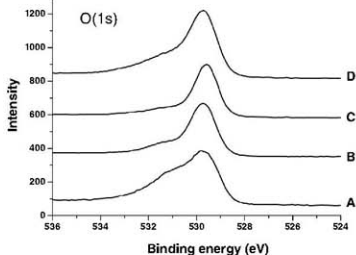
deduce that it is primarily the 0.5-nm bilayer clusters, rather than 0.2- to 0.3-nm monolayer Au clusters, that are active for CO oxidation on FeO$_x$ supports.

References and Notes

1. M. Haruta, *CATTECH* **6**, 102 (2002).
2. M. Haruta, *Gold Bull.* **37**, 27 (2004).
3. A. S. K. Hashmi, G. J. Hutchings, *Angew. Chem. Int. Ed.* **45**, 7896 (2006).
4. M. D. Hughes et al., *Nature* **437**, 1132 (2005).
5. D. I. Enache et al., *Science* **311**, 362 (2006).
6. A. Corma, P. Serna, *Science* **313**, 332 (2006).
7. J. Guzman, S. Carrettin, A. Corma, *J. Am. Chem. Soc.* **127**, 3286 (2005).
8. J. J. Pietron, R. M. Stroud, D. R. Rolison, *Nano Lett.* **2**, 545 (2002).
9. J. Guzman, B. C. Gates, *J. Am. Chem. Soc.* **126**, 2672 (2004).
10. G. J. Hutchings et al., *J. Catal.* **242**, 71 (2006).
11. M. M. Schubert et al., *J. Catal.* **197**, 113 (2001).
12. R. Meyer, C. Lemire, Sh. K. Shaikhutdinov, H.-J. Freund, *Gold Bull.* **37**, 72 (2004).
13. M. Valden, X. Lai, D. W. Goodman, *Science* **281**, 1647 (1998).
14. M. S. Chen, D. W. Goodman, *Science* **306**, 252 (2004), published online 26 August 2004; 10.1126/science.1102420.
15. D. Matthey et al., *Science* **315**, 1692 (2007).
16. N. A. Hodge et al., *Catal. Today* **72**, 133 (2002).
17. Materials and methods are available as supporting material on *Science* Online.
18. M. Varela et al., *Annu. Rev. Mater. Res.* **35**, 539 (2005).
19. C. W. Mays et al., *Surf. Sci.* **12**, 134 (1968).
20. S. Wang et al., *Nat. Mater.* **3**, 143 (2004).
21. T. V. W. Janssens et al., *Top. Catal.* **44**, 15 (2007).
22. W. Yan et al., *J. Phys. Chem. B* **109**, 10676 (2005).
23. H. Falsig et al., *Angew. Chem. Int. Ed.* **47**, 4835 (2008).
24. S. Rashkeev et al., *Phys. Rev. B* **76**, 035438 (2007).
25. A. Bongiorno, U. Landman, *Phys. Rev. Lett.* **95**, 106102 (2005).
26. M. Abu Haija et al., *Surf. Sci.* **600**, 1497 (2006).
27. B. Yoon et al., *Science* **307**, 403 (2005).
28. H. Hakkinen et al., *Angew. Chem. Int. Ed.* **42**, 1297 (2003).
29. V. A. Bondzie et al., *Catal. Lett.* **63**, 143 (1999).
30. We thank the Athena project of the Engineering and Physical Sciences Research Council, NSF, NASA, and the National Research Council Postdoctoral Associate program for funding this work.

Laser Frequency Combs for Astronomical Observations

Tilo Steinmetz,[1,2] Tobias Wilken,[1] Constanza Araujo-Hauck,[3] Ronald Holzwarth,[1,2] Theodor W. Hänsch,[1] Luca Pasquini,[3] Antonio Manescau,[3] Sandro D'Odorico,[3] Michael T. Murphy,[4] Thomas Kentischer,[5] Wolfgang Schmidt,[5] Thomas Udem[1]*

A direct measurement of the universe's expansion history could be made by observing in real time the evolution of the cosmological redshift of distant objects. However, this would require measurements of Doppler velocity drifts of ~1 centimeter per second per year, and astronomical spectrographs have not yet been calibrated to this tolerance. We demonstrated the first use of a laser frequency comb for wavelength calibration of an astronomical telescope. Even with a simple analysis, absolute calibration is achieved with an equivalent Doppler precision of ~9 meters per second at ~1.5 micrometers—beyond state-of-the-art accuracy. We show that tracking complex, time-varying systematic effects in the spectrograph and detector system is a particular advantage of laser frequency comb calibration. This technique promises an effective means for modeling and removal of such systematic effects to the accuracy required by future experiments to see direct evidence of the universe's putative acceleration.

Recent cosmological observations suggest that the universe's expansion is accelerating. Several lines of evidence corroborate this, including results from distant supernovae (1, 2), the cosmic microwave background (3), and the clustering of matter (4, 5). However, the current observations are all essentially geometric in nature, in that they map out space, its curvature, and its evolution. In contrast, a direct and dynamical determination of the universe's expansion history is possible by observing the slow drift of cosmological redshifts, z, that is inevitable in any evolving universe (6). No particular cosmological model or theory of gravity would be needed to interpret the results of such an experiment. However, the cosmological redshift drift is exceedingly small and

difficult to measure; for currently favored models of the universe, with a cosmological constant parametrizing the acceleration, the redshifts of objects drift by less than ~1 cm s^{-1} year^{-1} (depending on their redshifts).

Nevertheless, the suggestion that the so-called Lyman-α "forest" seen in high-redshift quasar spectra is the best target for this experiment (7) was recently supported by cosmological hydrodynamical simulations (8). The forest of absorption lines is caused by the Lyman-α transition arising in neutral hydrogen gas clouds at different redshifts along the quasar sight-lines. With simulated quasar spectra show that the planned 42-m European Extremely Large Telescope (E-ELT), equipped with the proposed Cosmic Dynamics Experiment (CODEX) spectrograph (9), could detect the redshift drift convincingly with 4000 hours of observing time over a ~20-year period (8). Therefore, as the observation is feasible (in principle), overcoming the many other practical challenges in such a measurement is imperative. Important astrophysical and technical requirements have been considered in detail, and most are not difficult to surmount (8, 10). One (but not the only) extremely important requirement is

that the astronomical spectrographs involved must have their wavelength scales calibrated accurately enough to record ~1 cm s^{-1} velocity shifts (~25-kHz frequency shifts) in the optical range. Moreover, this accuracy must be repeatable over ~20-year time scales.

Although the redshift drift experiment requires demanding precision and repeatability, precisely calibrated astronomical spectrographs have several other important applications. For example, Jupiter- and Neptune-mass extrasolar planets have been discovered by the reflex Doppler motion of their host stars (11–13), but detecting Earth-mass planets around solar-mass stars will require ~5 cm s^{-1} precision maintained over several-year time scales (14). Another example is the search for shifts in narrow quasar absorption lines caused by cosmological variations in the fundamental constants of nature (15–17). Recent measurements (18–21) achieve precisions of ~20 m s^{-1}, but the possibility of hidden systematic effects, and the increased photon-collecting power of future ELTs, warrant much more precise and accurate calibration over the widest possible wavelength range.

Laser frequency combs (LFCs) offer a solution because they provide an absolute, repeatable wavelength scale defined by a series of laser modes equally spaced across the spectrum. The train of femtosecond pulses from a mode-locked laser occurs at the pulse repetition rate, f_{rep}, governed by the adjustable laser cavity length. In the frequency domain, this yields a spectrum, $f_n = f_{ceo} + n \times f_{rep}$ with modes enumerated with an integer $n \sim 10^5$ to 10^6. The carrier envelope offset frequency, $f_{ceo} \leq f_{rep}$, accounts for the laser's internal dispersion, which causes the group and phase velocities of the pulses to differ (22). Thanks to the large integer n, the optical frequencies f_n are at hundreds of THz whereas both f_{rep} and f_{ceo} are radio frequencies and can be handled with simple electronics and stabilized by an atomic clock (22). Each mode's absolute frequency is known to a precision limited only by the accuracy of the clock. Even low-cost, portable atomic clocks provide ~1 cm s^{-1} (or 3 parts in 10^{11}) precision. Because LFC light power is much higher than required, the calibration precision possible is therefore limited by the maximum signal-to-noise

[1]Max-Planck Institut für Quantenoptik, Hans-Kopfermann-Strasse 1, D-85748 Garching, Germany. [2]Menlo Systems GmbH, Am Klopferspitz 19, D-82152 Martinsried, Germany. [3]European Southern Observatory, Karl-Schwarzschild-Strasse 3, D-85748 Garching, Germany. [4]Centre for Astrophysics and Supercomputing, Swinburne University of Technology, Mail H39, Post Office Box 218, Victoria 3122, Australia. [5]Kiepenheuer-Institut für Sonnenphysik, Schöneckstr. 6, D-79104 Freiburg, Germany.

*To whom correspondence should be addressed. E-mail: thu@mpq.mpg.de

ratio (SNR) achievable with the detector. For modern astronomical charge-coupled devices (CCDs), the maximum SNR in a single exposure is limited by their dynamic range but is still sufficient to achieve ~1 cm s^{-1} precision (23). Furthermore, because LFC calibration is absolute, spectra from different epochs, or even different telescopes, can be meaningfully compared.

The main challenge in reaching ~1 cm s^{-1} calibration accuracy will be the measurement and, eventually, mitigation and/or modeling and removal of systematic effects in astronomical spectrographs and detectors. For typical high-resolution spectrographs, a ~1 cm s^{-1} shift corresponds roughly to the physical size of a silicon atom in the CCD substrate. Only with the statistics of a very large number of calibration lines can the required sensitivity be achieved, provided that systematic effects can be controlled accordingly (10). For example, even in a highly stabilized, vacuum-sealed spectrograph, small mechanical drifts will slightly shift the spectrum across the CCD. Although this can easily be tracked to first order, other effects such as CCD intrapixel sensitivity variations will be important for higher precision. Discovering, understanding, and eventually modeling and removing these effects is crucial for the long-term goal of accurate calibration; tests of LFCs on astronomical telescopes, spectrographs, and detectors are therefore imperative.

We have conducted an astronomical LFC test on the German Vacuum Tower Telescope (24) (VTT) (Fig. 1). We used a portable rubidium clock with a modest accuracy of 5 parts in 10^{11} (or 1.5 cm s^{-1}); much more accurate clocks are available if needed. This sets the absolute uncertainty on the frequency of any given comb mode. The VTT can be operated at near-infrared wavelengths, thereby allowing a relatively simple and reliable fiber-based LFC to be used. The erbium-doped fiber LFC used had $f_{rep} = 250$ MHz which, despite the VTT spectrograph having higher resolving power (resolution of 0.8 GHz or 1.2 km s^{-1}) than most astronomical spectrographs, is too low for modes to be resolved apart. Filtering out unwanted modes by using a Fabry-Pérot cavity (FPC) outside the laser (25, 26) was suggested as one solution (23, 27) and has proven effective (28, 29). The FPC comprises two mirrors separated by a distance smaller than the laser cavity length so that all modes, except every mth ($m > 1$), are interferometrically suppressed (Fig. 1, lower panel). We used a FPC stabilized to a filter ratio, m, by controlling its length with an electronic servo system to generate effective mode spacings, $m \times f_{rep}$, between 1 and 15 GHz. The degree to which the unwanted modes are suppressed is an important parameter. The FPC transmission function falls sharply away from the transmitted mode frequencies but, because nearby suppressed modes are not resolved from the transmitted ones by the spectrograph, small asymmetries in this function (especially combined with time variations) can cause systematic shifts in the measured line positions. With our setup, we achieve an unwanted mode sup-

pression of more than 46 dB at filter ratios $m \leq 20$. Other possible systematic shifts due to the filtering have been identified (29) and need to be controlled.

LFC spectra were recorded with and without the spectrum of a small section of the Sun's photosphere at wavelengths ~1.5 μm. A sample $m \times f_{rep} = $ 15-GHz recording, superimposed with Fraunhofer and atmospheric lines, is shown in Fig. 2. To estimate our calibration accuracy and to test the spectrograph's stability, we analyzed several exposures of the LFC only. Individual Lorentzian functions were fitted to the recorded modes as a function of pixel position and identified with the absolute comb frequencies, f_n, which are referenced to the atomic clock (10). The dense grid of modes allows the spectrograph's calibration function (Fig. 3A) to be determined to very high accuracy; even a simple, second-order polynomial fit to the pixel-versus-frequency distribution has only 9 m s^{-1} root mean square (RMS) residual deviations around it (Fig. 3B), and this remains almost unchanged with higher-order polynomial modeling (10).

With traditional calibration techniques, such as thorium comparison lamps, I$_2$ gas absorption cells or Earth's atmospheric absorption lines for calibration achieve ~10 m s^{-1} absolute precision per calibration line at best (30). Thus, even with these "first light" comb recordings, we already demonstrate superior absolute calibration accuracy. Because more than 10^4 modes will be available

in a larger-bandwidth LFC, the statistical uncertainty would be reduced to the 1 cm s^{-1} regime if the residuals were truly random. However, the theoretical shot noise limit calculated from the number of photons recorded per comb mode is much smaller than 9 m s^{-1}; systematic effects from the spectrograph and detector system evidently completely dominate the residuals.

The main reason for testing LFCs at real telescopes, on real astronomical spectrograph and detector systems, is to understand how to measure and then mitigate and/or model and remove such systematics. Because the VTT spectrograph is not stabilized (i.e., temperature-, pressure- and vibration-isolated), instrument drifts are expected and the VTT LFC spectra can already be used to track them accurately. From a time series of exposures, we derive a drift in the spectrograph of typically 8 m s^{-1} min^{-1} (5 MHz min^{-1}) (10). Much lower drift rates have been demonstrated with suitably stabilized instruments [e.g., ~1 m s^{-1} over months with HARPS (13)]; although the VTT is not optimized for stability, this does not affect its usefulness to test calibration procedures. Indeed, different modes are observed to drift at different rates, with neighboring modes having highly correlated drift rates (10). Also, as the comb modes drift across the detector, higher-order distortions are evident, which are the combined result of many effects, such as intrapixel
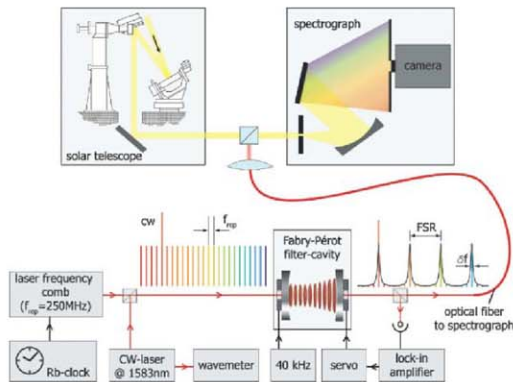

Fig. 1. Sketch of our experimental setup at the VTT. By superimposing the frequency comb with light from a celestial body—in this case, the Sun—one can effectively calibrate its emission or absorption spectrum against an atomic clock. An erbium-doped fiber LFC with 250-MHz mode spacing (pulse repetition rate) is filtered with a FPC to increase the effective mode spacing, allowing it to be resolved by the spectrograph. The latter has a resolution of ~0.8 GHz at wavelengths around 1.5 μm, where our LFC tests were conducted. The LFC was controlled by a rubidium atomic clock. A continuous-wave (CW) laser at 1583 nm was locked to one comb line and simultaneously fed to a wavemeter. Even though the wavemeter is orders of magnitude less precise than the LFC itself, it is sufficiently accurate (better than 250 MHz) to identify the mode number, n. The FPC length, defining the final free spectral range (FSR), was controlled by feedback from its output. See (10) for further details.

Fig. 2. Spectra of the solar photosphere (background image) overlaid by a LFC with 15-GHz mode spacing (white, equally spaced vertical stripes). Spectra are dispersed horizontally, whereas the vertical axis is a spatial cross section of the Sun's photosphere. The upper panel shows a small section of the larger portion of the spectrum below. The brighter mode labeled with its absolute frequency is additionally superimposed with a CW laser used to identify the mode number (Fig. 1). The frequencies of the other modes are integer multiples of 15 GHz higher (right) and lower (left) in frequency. Previous calibration methods would use the atmospheric absorption lines (dark vertical bands labeled "Atm" interleaved with the Fraunhofer

absorption lines), which are comparably few and far between. Also shown in the upper panel is the only thorium emission line lying in this wavelength range from a typical hollow-cathode calibration lamp. Recording it required an integration time of 30 min, compared with the LFC exposure time of just 10 ms. Unlike with the LFC, the thorium calibration method cannot be conducted simultaneously with solar measurements at the VTT. The nominal horizontal scale is 1.5×10^{-3} nm pixel^{-1} with ~1000 pixels shown horizontally in the upper panel. Black horizontal and vertical lines are artifacts of the detector array.
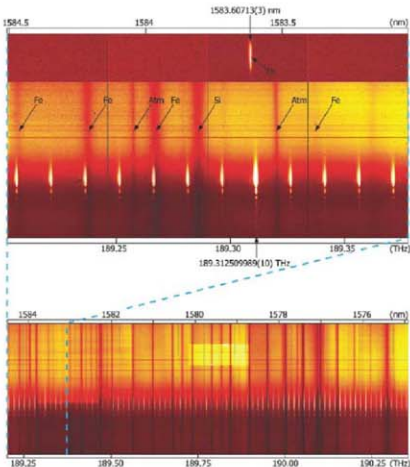
Fig. 3. Precision achieved with our calibration with a LFC filtered to 3 GHz ($m = 12$). (**A**) The position of the transmitted modes, derived from a multi-Lorentzian fit, plotted against the mode number. Modes without a corresponding detector position measurement were deemed unsuitable for use in calibration because they fell on large detector artifacts and/or were overlaid with light from the CW laser. The size of one pixel corresponds to 172 MHz at 1583 nm. On this scale, no distortions are visible. (**B**) The residuals from a quadratic fit that gives a RMS residual of 9 m s^{-1}. The quadratic fit greatly reduces the residuals compared to a linear model, whereas higher-order polynomials do not improve the performance of the fit significantly (10). Even with these first LFC recordings from the VTT, the 9 m s^{-1} RMS residuals here indicate better absolute calibration than is achieved with traditional calibration methods (30).
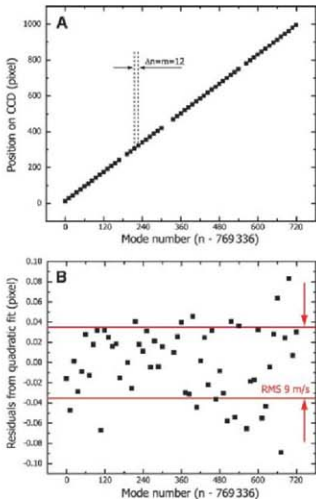
sensitivity variations. Thus, the VTT data already show an important advantage of LFC calibration: The dense grid of high SNR calibration information allows the discovery and measurement of complex effects correlated across the chip and in time.

The first light for frequency combs on astronomical spectrographs has delivered calibration precision beyond the state of the art. The key opportunity now is to use LFC spectra to measure and remove systematic effects in order to reach the ~1 cm s^{-1} long-term calibration precision, accuracy, and repeatability required to realize the redshift drift experiment.

References and Notes

1. A. G. Riess *et al.*, *Astron. J.* **116**, 1009 (1998).
2. S. Perlmutter *et al.*, *Astrophys. J.* **517**, 565 (1999).
3. D. N. Spergel *et al.*, *Astrophys. J.* **148** (suppl.), 175 (2003).
4. J. A. Peacock *et al.*, *Nature* **410**, 169 (2001).
5. D. J. Eisenstein *et al.*, *Astrophys. J.* **633**, 560 (2005).
6. A. Sandage, *Astrophys. J.* **136**, 319 (1962).
7. A. Loeb, *Astrophys. J.* **499**, L111 (1998).
8. J. Liske *et al.*, *Mon. Not. R. Astron. Soc.* **386**, 1192 (2008).
9. L. Pasquini *et al.*, in *Proceedings of the IAU Symposium*, P. Whitelock, M. Dennefeld, B. Leibundgut, Eds. (Cambridge Univ. Press, Cambridge, 2006), vol. 232, pp. 193–197.
10. Materials and methods are available as supporting material on Science Online.
11. M. Mayor, D. Queloz, *Nature* **378**, 355 (1995).
12. G. W. Marcy, R. P. Butler, *Astrophys. J.* **464**, L147 (1996).
13. C. Lovis *et al.*, *Nature* **441**, 305 (2006).
14. C. Lovis *et al.*, in *Proceedings of the SPIE*, I. S. McLean, I. Masanori, Eds. (2006), vol. 6269, pp. 62690P1–62690P9.
15. J. N. Bahcall, E. E. Salpeter, *Astrophys. J.* **142**, 1677 (1965).
16. J. K. Webb, V. V. Flambaum, C. W. Churchill, M. J. Drinkwater, J. D. Barrow, *Phys. Rev. Lett.* **82**, 884 (1999).
17. R. I. Thompson, *Astron. Lett.* **16**, 3 (1975).
18. M. T. Murphy, J. K. Webb, V. V. Flambaum, *Mon. Not. R. Astron. Soc.* **345**, 609 (2003).
19. H. Chand, R. Srianand, P. Petitjean, B. Aracil, *Astron. Astrophys.* **417**, 853 (2004).
20. S. A. Levshakov *et al.*, *Astron. Astrophys.* **449**, 879 (2006).
21. E. Reinhold *et al.*, *Phys. Rev. Lett.* **96**, 151101 (2006).
22. Th. Udem, R. Holzwarth, T. W. Hänsch, *Nature* **416**, 233 (2002).
23. M. T. Murphy *et al.*, *Mon. Not. R. Astron. Soc.* **380**, 839 (2007).
24. E. H. Schröter, D. Soltau, E. Wiehr, *Vistas Astron.* **28**, 519 (1985).
25. T. I. Sizer, *IEEE J. Quantum Electron.* **25**, 97 (1989).
26. Th. Udem, J. Reichert, R. Holzwarth, T. W. Hänsch, *Phys. Rev. Lett.* **82**, 3568 (1999).
27. P. O. Schmidt, S. Kimeswenger, H. U. Kaeufl, *Proc. 2007 ESO Instrument Calibration Workshop*, ESO Astrophysics Symposia series (Springer, in press); available at http://arxiv.org/abs/0705.0763.
28. C.-H. Li *et al.*, *Nature* **452**, 610 (2008).
29. D. A. Braje, M. S. Kirchner, S. Osterman, T. Fortier, S. A. Diddams, *Eur. Phys. J. D* **48**, 57 (2008).
30. C. Lovis, F. Pepe, *Astron. Astrophys.* **468**, 1115 (2007).
31. We thank the Kiepenheuer Institut für Sonnenphysik staff at the Vacuum Tower Telescope and the Instituto de Astrofísica de Canarias (IAC) personnel for their support during the measurements at the VTT. We especially appreciate the efforts of M. Collados (IAC) and F. Kerber (ESO). We thank T. Kippenberg for CW-laser assistance and J. Liske for advice on the manuscript. M.T.M. thanks the Australian Research Council for a QEII Research Fellowship (DP0877998).

Regional Synthesis of Mediterranean Atmospheric Circulation During the Last Glacial Maximum

J. Kuhlemann,[1]* E. J. Rohling,[2] I. Krumrei,[1] P. Kubik,[3] S. Ivy-Ochs,[4] M. Kucera[1]

Atmospheric circulation leaves few direct traces in the geological record, making reconstructions of this crucial element of the climate system inherently difficult. We produced a regional Mediterranean synthesis of paleo-proxy data from the sea surface to alpine altitudes. This provides a detailed observational context for change in the three-dimensional structure of atmospheric circulation between the Last Glacial Maximum (LGM, ~23,000 to 19,000 years ago) and the present. The synthesis reveals evidence for frequent polar air incursions, topographically channeled into the northwestern Mediterranean. Anomalously steep vertical temperature gradients in the central Mediterranean imply local convective precipitation. We find the LGM patterns to be analogous, though amplified, to previously reconstructed phases of enhanced meridional winter circulation during the Maunder Minimum (the Little Ice Age).

Mediterranean climate is determined by an interplay between atmospheric and marine processes and strongly differentiated regional topography (1). A wealth of paleoclimate data is available from archives recording conditions at the sea surface and on land at various altitudes, making the Mediterranean one of the few regions in the world where the thermal and dynamical structure of the lower atmosphere could be reconstructed for certain past intervals (2). Such reconstructions are invaluable for validation of the atmospheric component in climate models (3). Recent attempts to compare model simulations with regional proxy data over Europe during the Last Glacial Maximum (LGM) revealed substantial disagreement, both among the models and between models and paleodata (4, 5), highlighting the need for model-independent constraints on past regional climatic patterns.

The state of the atmosphere in the past is inherently difficult to reconstruct. Proxies from oceanic sediments record mainly large-scale atmospheric patterns (6); and terrestrial proxy data, such as those from peat bogs or lake sediments, can be biased by local climate, including temperature inversion and interannual variability (7, 8). The equilibrium line altitude (ELA) of glaciers contains information on the vertical structure of the atmosphere, which can be reconstructed by in situ dating of glacial advances and retreats. Small temperate glaciers in circum-Mediterranean mountain chains are (and were) exposed to well-mixed air masses and are known to have been sensitive to even small changes of the ELA, typically responding by advancing or retreating within periods ranging from several years to decades (9, 10).

The ELA responds to both temperature and precipitation change (9, 10), and it is possible to differentiate between these two factors only in particularly well-studied regions, such as Corsica (data supplement S1 and figs. S2 and S3). For Corsica, we present new information on the LGM ELA, including a deconvolution of the two main controlling processes (figs. S4, B and C). For the ELA depression of LGM glaciers in the wider Mediterranean region, we used previously published information (table S2), which, as a first-order end-member solution, we calculated as pure temperature change, using a standard free atmospheric lapse rate of a 6.5°C decrease per kilometer (6.5°C/km) of increasing elevation. The potential overprint of precipitation changes was then considered where anomalous results were found. The error ranges on the resultant ELA reconstructions

(Fig. 1) amount to up to ±100 m in Corsica and ±150 m in other Mediterranean mountains (fig. S1 and Fig. 2). We thus developed a regional synthesis of glacial vertical temperature gradients in the lower atmosphere. Paleoflora-based temperature reconstructions for a variety of terrestrial sites at lower altitudes around the Mediterranean (7, 8) (Fig. 2 and fig. S3) were used to validate and complement our ELA-based temperature reductions and precipitation patterns.

Next, we compared the ELA-based LGM cooling at alpine altitudes with estimates of LGM reduction of Mediterranean sea surface temperatures (SSTs) derived from the difference between long-term instrumental averages (11) and glacial SST reconstructions based on foraminiferal assemblages (12, 13) and alkenone data (14) (Figs. 1 and 2). Such direct comparison between SST and ELA changes is warranted for the Mediterranean basin, where SSTs generally are closely related to air temperature and the insolation/radiation balance (15).

The combination of data on glacial cooling at sea level (SST proxies) and higher altitudes (ELA depression) provides direct constraints on the vertical structure of the LGM atmosphere. When comparing the temperature equivalent of the ELA depression with SST reduction in the LGM relative to the present (Fig. 2), we consider that a shift of similar magnitude would indicate a constant atmospheric lapse rate. Stronger relative reduction of SST would imply a lapse rate of less than 6.5°C/km, supporting more stable atmospheric stratification. A lesser relative SST reduction would imply a lapse rate steeper than 6.5°C/km, potentially enhancing the instability of the atmosphere, driving convection and consequent precipitation.

Our analysis (figs. S1 and S2) reveals an LGM pattern of southward-extending lobes of ELA depression in mountainous regions of Italy
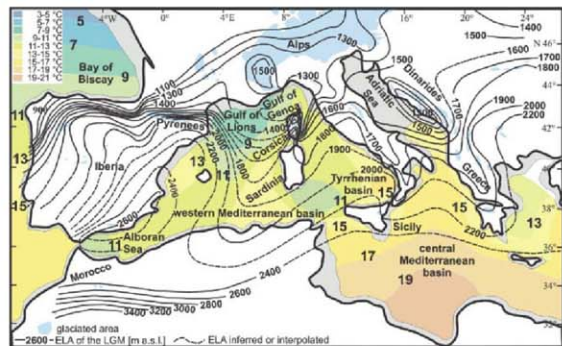

Fig. 1. Map of the ELA in the western-central Mediterranean region during the phase of maximum glacier expansion during the LGM (probably at ~23,000 years before the present) and of average annual SSTs and ELA during the LGM. The error range of the ELA estimate is ±150 m for the Mediterranean in general and ±100 m in Corsica.

[1]Institute for Geosciences, University of Tuebingen, Sigwartstrasse 10, D-72076 Tuebingen, Germany. [2]School of Ocean and Earth Science, National Oceanography Centre, Southampton SO14 3ZH, UK. [3]Institute of Particle Physics, HPK H30, ETH Zurich, CH-8093 Zurich, Switzerland. [4]Institute of Particle Physics, HPK H27, ETH Zurich, CH-8093 Zurich, Switzerland.

*To whom correspondence should be addressed. E-mail: kuhlemann@uni-tuebingen.de

and the Dinarides, which suggests frequent higher-altitude southward advances of polar air (Fig. 1). Iberia is characterized by a steep gradient from the northern and northwestern coastlines toward the interior and southeast, which probably results predominantly from barrier effects of near-coastal mountain ranges (Fig. 1). The data from Corsica especially identify a lobe of ELA depression that extends over the Gulf of Lions toward the south and east (Fig. 1), indicating a substantial invasion of polar air from the north. The temperature difference inferred from the recent ELA (16) and our LGM reconstruction (fig. S3) generally decreases from north (10° to 11°C) to south (6° to 7°C) (Fig. 2), in agreement with previous reconstructions of a steeper glacial meridional temperature gradient (16, 18). The temperature differences calculated from the glacial ELA depression, relative to the present, generally agree with lower-altitude temperature reconstructions from paleofloral data (7, 8) (Fig. 2).

The present-day SST distribution and surface circulation in the western Mediterranean basin are strongly affected by northwesterly winds, particularly in the Gulf of Lions (15). As a consequence, cool waters are frequently upwelling in the Gulf of Lions (10° to 15°C). Surface currents are deflected by coastlines, and their strength and flow direction vary seasonally in response to surface winds and the superimposed atmospheric circulation (11, 15). Glacial SST values calculated from foraminiferal assemblages (12, 13) and alkenone data (14) display a roughly similar distribution to that of modern SSTs, albeit with a stronger westeast gradient due to stronger cooling in the northwestern Mediterranean than in the central and

eastern parts of the basin (12) (Fig. 1 and data supplement S3). The extraordinary cooling centered on the Gulf of Lions suggests frequent and/or more persistent northerly incursions of cold polar air, probably channeled through the Rhone valley at low elevation (14, 18), and between the glaciated Alps and the Pyrenees at higher elevation, as suggested by our ELA reconstructions.

Figure 2 compares the spatial pattern of the LGM reduction of SST (relative to the present) with that of atmospheric temperature as derived from our ELA reconstruction. This reveals that both SST and ELA-determined atmospheric temperatures (T_{ELA}) underwent similar (within ±2°C) changes, relative to the present, across the northern Bay of Biscay and the western sector of the western Mediterranean. LGM SST seems less reduced than T_{ELA} in the Atlantic Ocean offshore of Iberia and Morocco, which probably reflects the southward displacement of the relatively warm Gulf Stream during glacial times (3–6, 13, 19). In the central and (to a lesser extent) eastern Mediterranean, glacial SST appears to have dropped considerably less than T_{ELA} (Fig. 2). The notable warm anomaly in the central basin can hardly be attributed to the advection of warm surface waters from the western basin because of land barriers. In fact, a notable cool SST anomaly is seen to the southeast of Sardinia, which may reflect leeward upwelling triggered by northwesterly winds (Fig. 1). We propose that the advection of warm desert air from the Sahara and relatively cloud-free subtropical conditions over the central/eastern basin largely account for the minor LGM cooling of SSTs in this region. The fact that glacial SST dropped considerably less than calculated T_{ELA} over part of the Mediterranean suggests that the atmospheric lapse rate had noticeably steepened: up to ~10°C/km north of Corsica, ~9°C/km in the southern Adriatic Sea, and ~8.5°C/km in the central Mediterranean. Given that we applied an initial end-member ELA transformation to (only) temperature changes, using a standard lapse rate of 6.5°C/km, it is clear that increased convective precipitation must be inferred to explain the noticeably steeper rates diagnosed in these specific regions.

The spatial distributions of SST, T_{ELA}, and of the SST-T_{ELA} difference in the western-central Mediterranean during the LGM are found to be roughly similar to those in the present, although meridional gradients were enhanced during the LGM (Figs. 1 and 2). Hence, it is not unreasonable to expect that cyclones followed similar preferential storm tracks across the basin as well, which contrasts with previous suggestions of northeast-directed cyclone tracks from the Alboran Sea toward the southern flank of the Alps (20). During cold periods such as the LGM, cold northerly air outbreaks over the western basin were probably more frequent (12, 17, 18). The pronounced southward cold (polar air) expansion toward northwest Africa (Figs. 1 and 2) would have triggered cyclogenesis over the relatively warm Mediterranean waters, causing flows of desert air toward the north and northeast, as indicated by the north-extending lobe of the ELA in southeastern Europe (Fig. 1). This would be consistent with observations of enhanced wind-blown dust supply from the Sahara into the eastern Mediterranean during glacial times (21).

Even though we compare glacial conditions (the LGM) with interglacial conditions (the present), we observe that the reconstructed property distribution patterns, particularly the preferential flow of polar air masses, are pervasive through time (Figs. 1 and 2). Indeed, these features appear to be strongly fixed by the land/sea distribution and topography, which are virtually invariant on the time scales considered. Outbreaks of polar air masses over the western Mediterranean are typically funneled between the Alps and the Pyrenees, both at present and during the LGM, causing conditions conducive to cyclogenesis over the Gulf of Genoa. The funneling effect may have been stronger with glaciated mountains, as the ice rose several hundreds of meters above the lower watersheds (20), and Arctic air masses would also have invaded the western Mediterranean more frequently and/or persistently than today, because of the more southerly position of the polar front during the LGM (3–5, 19, 22). The incursion of cold air masses would have favored the convection of moist air, especially in regions with relatively warm (less reduced) SST, so that we would predict considerable local LGM precipitation in Corsica, the Apennines, the Dinarides, and Greece, especially at the upwind flank of mountain ranges and close to the coast. This would be a suitable mechanism to explain steeper horizontal precipitation gradients during the LGM relative to the present, which indeed are suggested by our data for the steep mountainous margins of northern
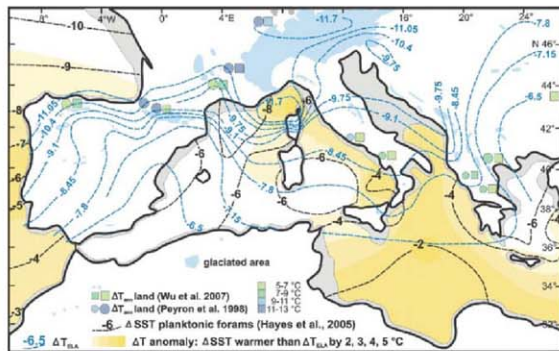

Fig. 2. Map of the temperature difference between recent and LGM SSTs (in black) and the temperature equivalent of the ELA depression (6.5°C/km lapse rate; in blue), respectively. The error range of this estimate is ±1°C for the Mediterranean in general and ±0.7°C in Corsica. In orange-colored marine regions, LGM SSTs were lowered significantly less than temperatures in the mid-troposphere, relative to the present. This implies an anomalously steep lapse rate and unstable layering of the lower troposphere. Atmospheric cooling values for low-elevation terrestrial sites based on paleofloral estimates are given for comparison. Small symbols indicate larger error and large symbols lesser error of the temperature estimate. Δ, change in.

Corsica (table S1 and fig. S1). This island's dry northern interior today receives ~30% less precipitation than its margins (fig. S2A), whereas this difference was ~50% during the LGM (fig. S4C). Although this prediction cannot (yet) be confirmed with the data available outside Corsica, it does agree with patterns seen in LGM reconstructions with the high-resolution climate model HadRM (23). As mentioned above, locally enhanced precipitation would largely reduce the local lapse rate, so that much of the initially (first-order) inferred temperature anomaly pattern in fact reflects the impact of precipitation anomalies.

Although care must be taken not to simply ascribe past regional property distributions to modern climate oscillation patterns (24), it remains useful to consider instrumental records and proxy data in order to develop a sense of realistic analogous climate patterns over the study region (25). The contrast between strongly reduced SST in the western basin and much less reduced SST in the central Mediterranean basin during the LGM (Fig. 1) indicates a preferentially meridional geostrophic circulation, with a polar trough that frequently protruded into the western Mediterranean. Such a circulation is favored by northward extension of the Azores High toward Iceland (North Atlantic ridge) or Greenland, blocking moisture supply by the westerlies. It is further enhanced by expansion and intensification of the Siberian High in winter during glacial times (26). A similar configuration is thought to have been common during the late Little Ice Age, notably the Maunder Minimum (2, 27). The invasion of polar air as shown by our data, channeled by the topography of mountain ranges and ice sheets in Europe,

would have generated cyclone formation in the Gulf of Genoa more frequently than at present, enhancing precipitation along various storm tracks in easterly directions. Our observations do not support a straightforward zonal LGM atmospheric circulation, as inferred from climate models (19, 28). Instead, we propose that frequent meridional circulation during cold seasons (characterized by the LGM ELA pattern) may have alternated with more zonal circulation during warm seasons. A more comprehensive quantitative assessment of the preferential LGM atmospheric circulation requires the use of both nested model simulation and high-resolution global climate model studies (4, 5, 8, 28), which should fully resolve the changing topography of glaciated mountain ranges and ice sheets. The validation of such models with our three-dimensional LGM climate proxy data ranging from the sea surface to alpine altitudes is a great future challenge.

References and Notes

1. E. Xoplaki, J. F. Gonzalez-Rouco, J. Luterbacher, H. Wanner, Clim. Dyn. 23, 63 (2004).
2. J. Luterbacher et al., in The Mediterranean Climate: An Overview of the Main Characteristics and Issues, P. Lionello, P. Malanotte-Rizzoli, R. Boscolo, Eds. (Elsevier, Amsterdam, 2006), pp. 27–148.
3. COHMAP Members, Science 241, 1043 (1988).
4. M. Kageyama et al., Quat. Sci. Rev. 25, 2082 (2006).
5. G. Ramstein et al., Clim. Past 3, 331 (2007).
6. G. Bond et al., Nature 365, 143 (1993).
7. O. Peyron et al., Quat. Res. 49, 183 (1998).
8. H. Wu, J. Guiot, S. Brewer, Z. Guo, Clim. Dyn. 29, 211 (2007).
9. H. Kerschner, G. Kaser, R. Sailer, Ann. Glaciol. 31, 80 (2000).
10. D. Steiner et al., Clim. Change, 10.1007/s10584-008-9393-1 (2008).
11. M. Conkright et al., World Ocean Atlas 1998 CD ROM Data Set Documentation (Technical Report 15, NODC Internal Report, Silver Spring, MD, 1998).
12. A. Hayes, M. Kucera, N. Kallel, L. Sbaffi, E. J. Rohling, Quat. Sci. Rev. 24, 999 (2005).
13. A. Paul, C. Schäfer-Neth, Palaeoceanography 18, 1058 (2003).
14. I. Cacho, J. O. Grimalt, M. Canals, J. Mar. Syst. 33-34, 253 (2002).
15. N. Pinardi, E. Masetti, Palaeogeogr. Palaeoclimatol. Palaeoecol. 158, 153 (2000).
16. B. Messerli, Geogr. Helv. 22, 105 (1967).
17. V. Masson-Delmotte et al., Clim. Dyn. 26, 513 (2006).
18. E. J. Rohling, A. Hayes, D. Kroon, S. De Rijk, W. J. Zachariasse, Palaeoceanography 13, 316 (1998).
19. M. Kageyama, F. D. Andrea, G. Ramstein, P. J. Valdes, R. Vautard, Clim. Dyn. 15, 773 (1999).
20. D. Florineth, C. Schlüchter, Quat. Res. 54, 295 (2000).
21. J. C. Larrasoana, A. P. Roberts, E. J. Rohling, M. Winklhofer, R. Wehausen, Clim. Dyn. 21, 689 (2003).
22. U. Pflaumann et al., Palaeoceanography 18, 10.1029/2002PA000774 (2003).
23. A. Jost et al., Clim. Dyn. 24, 577 (2005).
24. F. Justino, W. R. Peltier, Geophys. Res. Lett. 32, 10.1029/2005GL023822 (2005).
25. C. Cassou, L. Terray, J. W. Hurrell, C. Deser, J. Clim. 17, 1055 (2004).
26. E. J. Rohling, P. A. Mayewski, P. Challenor, Clim. Dyn. 20, 257 (2003).
27. J. Jacobeit, P. Jönsson, L. Bärring, C. Beck, M. Ekström, Clim. Change 48, 219 (2001).
28. A. Laîné et al., Clim. Dyn., 10.1007/s00382-008-0391-9 (2008).
29. We gratefully acknowledge funding from the German Science Foundation (DFG project KU1298/7) and the UK Natural Environment Research Council's thematic program Quantifying the Earth System (QUEST).

Kinematic Constraints on Glacier Contributions to 21st-Century Sea-Level Rise

W. T. Pfeffer,[1]* J. T. Harper,[2] S. O'Neel[3]

On the basis of climate modeling and analogies with past conditions, the potential for multimeter increases in sea level by the end of the 21st century has been proposed. We consider glaciological conditions required for large sea-level rise to occur by 2100 and conclude that increases in excess of 2 meters are physically untenable. We find that a total sea-level rise of about 2 meters by 2100 could occur under physically possible glaciological conditions but only if all variables are quickly accelerated to extremely high limits. More plausible but still accelerated conditions lead to total sea-level rise by 2100 of about 0.8 meter. These roughly constrained scenarios provide a "most likely" starting point for refinements in sea-level forecasts that include ice flow dynamics.

Eustatic land ice contributions to sea-level change come from surface mass balance (SMB) losses and discharge of ice into the ocean through marine-terminating glaciers. Dynamically forced discharge, via fast flow and calving of marine-terminating glaciers allowing rapid land-to-ocean transfer of ice, is well known from studies of temperate marine-terminating glaciers

(1–4) and is observed in Greenland (5–7). The consensus estimate of sea-level rise (SLR) by 2100 (0.18 to 0.6 m) that was published in the Intergovernmental Panel on Climate Change (IPCC) Fourth Assessment (8) excluded dynamic effects on the grounds that present understanding of the relevant processes is too limited for reliable model estimates. Because modeling (9) and paleo-

climate comparisons (10) have yielded multimeter per century estimates of SLR, similar increases have been inferred as a viable 21st-century scenario. Also argued is that feedbacks unaccounted for in the IPCC estimate could quickly cause several meters of very rapid SLR (11, 12).

Accurate SLR forecasts on the century time scale are imperative for planning constructive and cost-effective responses. Underestimates will prompt inadequate preparation for change, whereas overestimates will exhaust and redirect resources inappropriately. Raising California Central Valley levees only 0.15 m, for example, will cost over $1 billion (13); the nonlinearly increasing costs of raising levees 2 m or more without clear and compelling cause would entail enormous expenditures otherwise used for different responses as demanded by a smaller but still significant SLR.

We address the plausibility of very rapid SLR from land ice occurring this century. We give

[1]Institute of Arctic and Alpine Research, University of Colorado, Boulder, CO 80309, USA. [2]Department of Geosciences, University of Montana, Missoula, MT 59812, USA. [3]Scripps Institution of Oceanography, University of California San Diego, San Diego, CA 92093, USA.

*To whom correspondence should be addressed. E-mail: pfeffer@tintin.colorado.edu

particular emphasis to Greenland because of its vulnerability to ongoing Arctic warming and meltwater-related feedbacks, recent accelerations of ice motion, and its large volume reductions during the last interglacial (14). By using a simple kinematic approach, we determined Greenland and Antarctic outlet glacier velocities required to achieve various magnitudes of SLR by 2100.

To begin, we postulated sea-level increases of 2 and 5 m by 2100 forced solely by Greenland. The total water mass losses required to achieve these targets are 7.24×10^5 Gt and 1.81×10^6 Gt, respectively (Table 1). Of this mass, 2.58×10^4 Gt (less than 4% of the total for 2 m SLR) will be lost as SMB by 2100, which we estimated by integrating present-day values of mass loss forward at present-day rates of change (15), with present-day SMB estimated at 30% of total present-day rate of mass loss (5). Because future SMB is highly uncertain, we also scaled total SMB losses up by a factor of 10 to investigate the effect of uncertainty in SMB. Adjusting total mass losses for SMB contributions yields the mass to be discharged through marine-based outlets (Table 1). Even when scaled up by an order of magnitude, SMB is a very small fraction of the total loss required to produce the targeted SLR. Thus, even large uncertainties in future SMB have little influence on this calculation.

Rapid, dynamically unstable discharge of ice through calving is restricted to glaciers with beds based below sea level. We identified and calculated the aggregate cross-sectional area of Greenland's marine-terminating outlet glaciers by using surface and bed topography (16) and measured ice velocities (5) to identify all potential pathways for rapid discharge, including channels presently flowing rapidly as well as potentially unstable channels (Fig. 1 and table S1). Cross-sectional areas (gates) for each outlet were calculated at the point of greatest lateral constriction by bedrock in the glacier's marine-based reach. Ice stream widths in Antarctica can vary in time, but for Greenland outlet glaciers cross-sectional areas are constrained almost entirely by bedrock topography. Of the 290 km² total aggregate gate cross-sectional area, we identified 170 km² as the aggregate marine-based gate area where drainage to the ocean is not blocked by near-coastal sills standing above present-day sea level. All dynamic discharge (Table 2) must pass through these gates by 2100 to meet 2- to 5-m SLR targets. We considered four scenarios: velocities were calculated for both the "marine-based" gate (170 km²) and the "total aggregate" gate (290 km²) given both projected SMB and 10× inflated SMB losses. We then considered whether those velocities are realistic.

Coarseness of the digital elevation models (DEMs) used for surface and bed topography (16) led to uncertainties in the calculated gate areas, which may be substantial but cannot be evaluated directly. We accounted for a potential underestimate of gate area with a calculation using the total aggregate gate area. The total aggregate area exceeds the more relevant marine-based gate area

by 70%. Uncertainties arising from the DEM more likely conceal small unresolved channels than large ones, so the actual gate areas may be smaller than we calculate (thus yielding higher velocities).

The present-day average velocity of all Greenland outlet glaciers is 0.56 km/year when weighted

by drainage basin area or 1.23 km/year when weighted by gate cross-sectional area. The two weighted averages are different because gate cross-sectional area does not scale with drainage basin area. Average (present day to 2100) outlet glacier speeds required to meet 2- and 5-m SLR targets

Table 1. Fluxes and discharges for SLR targets. Q indicates total discharge to 2100 (Gt); q, Q converted to ice flux rate, total to 2100 (km³/year); Q_1, total dynamic discharge less SMB to 2100 (Gt); q_1, Q_1 converted to ice flux rate, total dynamic flux less SMB to 2100 (km³/year); Q_2, total dynamic discharge less 10× SMB to 2100 (Gt); and q_2, Q_2 converted to ice flux rate, total dynamic flux less 10× SMB to 2100 (km³/year).

SLR target	SLR mm/year	Q	q	Q_1	q_1	Q_2	q_2
2 m	21.5	724,000	8,650	698,164	8,341	652,464	7,795
5 m	53.8	1,810,000	21,625	1,784,165	21,317	1,738,464	20,770
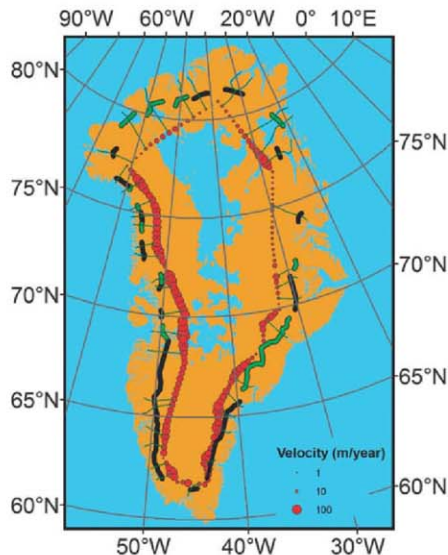
Fig. 1. Map showing Greenland and outlet glacier gates; marine-based gates are shown as dark green and nonmarine as black. Regions below sea level are colored blue. Ice velocities at ~2000 m elevation from (21) shown by red dots.

Table 2. Required velocities of Greenland gates for SLR targets.

SLR target	Present-day marine-based gates (km/year) 1× SMB	All present-day discharge gates (km/year) 1× SMB	Present-day marine-based gates (km/year) 10× SMB	All present-day discharge gates (km/year) 10× SMB
2 m	49	28.7	45.8	26.8
5 m	125	73.4	122	71.5

range from 26.8 km/year to 125 km/year, depending on the scenario considered [Table 2 and supporting online material (SOM)]. These velocities must be achieved immediately on all outlets considered and held at that level until 2100. Delays in the onset of rapid motion increase the required velocity further (fig. S1).

The scenario velocities far exceed the fastest motion exhibited by any Greenland outlet glacier. For example, the near-doubling of ice discharge from Jakobshavn Glacier in 2004–2005 was associated with an acceleration to 12.6 km/year (7). Similarly, a temporary 80% increase in the speed near the terminus of Kangerdlugssuaq produced a velocity of 14.6 km/year (6). A comparison of calculated (Table 2) and observed (1.23 km/year) average velocities shows that calculated values for a 2-m SLR exceed observations by a factor of 22 when considering all gates and inflated SMB and by a factor of 40 for the marine gates without inflated SMB, which we consider to be the more likely scenario. With the exception of discharge through all gates at inflated SMB (26.8 km/year), none of the velocity magnitudes shown in Table 2 has ever been observed anywhere, even over short time periods. The highest observed velocities have occurred at surging glaciers, including circa (ca.) 70 m/day (25.5 km/year) at Variegated Glacier (17) and 105 m/day (38.3 km/year) at Medvezhiy Glacier (18), but were held only for brief periods (hours to days). Although no physical proof is offered that the velocities given in Table 2 cannot be reached or maintained over century time scales, such behavior lies far beyond the range of observations and at the least should not be adopted as a central working hypothesis.

Calculations are made only for Greenland because Greenland's outlet glaciers are well constrained by bed topography, which (despite the

Table 3. SLR projections based on kinematic scenarios. Thermal expansion numbers are from (22).

	SLR equivalent (mm)		
	Low 1	Low 2	High 1
Greenland			
Dynamics	93	93	467
SMB	71	71	71
Greenland total	165	165	538
Antarctica			
PIG/Thwaites dynamics	108		394
Lambert/Amery dynamics	16		158
Antarctic Peninsula dynamics	12		59
SMB	10		10
Antarctica total	146	128	619
Glaciers/ice caps			
Dynamics	94		471
SMB	80		80
GIC total	174	240	551
Thermal expansion	300	300	300
Total SLR to 2100	785	833	2008

uncertainties mentioned) is well known in comparison to much of the Antarctic Ice Sheet and the Antarctic Peninsula and virtually all of the marine-terminating glaciers and ice caps (GIC) exclusive of Greenland and Antarctica. In order to estimate how these constraints influence projections of total SLR to 2100, we calculated a zero-order range of eustatic SLR from all land ice sources. Because marine-grounded channels are not well defined in many other locations, we made approximations and scaling arguments to arrive at a range of values for total eustatic SLR and, including reasonable projections of steric SLR, a range of estimates of total SLR to 2100.

Most of the marine-based ice in West Antarctica is held behind the Ross and Filchner-Ronne ice shelves, which we consider unlikely to be removed by climate or oceanographic processes within the next century [e.g., (19)]. The Amundsen Coast basin [including Pine Island Glacier (PIG) and Thwaites Glacier], however, is not confined by large ice shelves and contains about 1.5 m sea level equivalent (5.43×10^5 Gt) (20). The aggregate cross-sectional gate area of PIG and Thwaites Glacier is ca. 120 km^2 (20). The average velocity in this region is 2 km/year (table S2), higher than the average velocity of all Antarctic ice streams [0.65 km/year (19)]. An average (present day to 2100) velocity of 53.6 km/year is required to discharge 1.5 m sea-level equivalent through the PIG and Thwaites glacier gates by 2100, again far greater than any observed glacier velocity.

We present three scenarios by combining likely projection methods that we believe roughly bracket the range of potential near-future SLR outcomes (SOM). These are not true limiting cases but give a good sense of the potential variability of total SLR due to dynamic discharge effects.

SLR scenario Low 1 represents a low-range estimate based on specific adjustments to dynamic discharge in certain potentially vulnerable areas. We assumed a doubling of outlet glacier velocities in Greenland and PIG/Thwaites within the first decade and no change from present-day discharge values at Lambert/Amery. SMB for Greenland, the Antarctic Peninsula, and GIC was accelerated at present-day rates of SMB change, and, lacking more directly applicable constraints, dynamic discharge for the Antarctic Peninsula and GIC was calculated by scaling dynamic discharge to SMB by using the ratio of 1.31 as computed for Greenland (SOM). The net result, including thermal expansion, is 785 mm by 2100 (Table 3).

A second low-range scenario (Low 2) shows the effect of varying our assumptions; for this, we simply integrated presently observed rates of change forward in time. We calculated Greenland's contribution as for Low 1 but accelerated the present-day net discharge for Antarctica (East/West/Antarctic Peninsula) forward at the present-day rate of change given by (19). The GIC contribution was also calculated by accelerating the present-day net discharge at the current rate of change, with values

from (15). The net result, including thermal expansion, is 833 mm by 2100 (Table 3).

SLR scenario High 1 combines all eustatic sources taken at high but reasonable values. No firm highest possible value can be determined for SMB or dynamics; the values chosen represent judged upper limits of likely behavior on the century time scale. Greenland SMB was accelerated at present-day rates of change, but dynamic discharge was calculated by accelerating outlet glacier velocities by an order of magnitude in the first decade. In Antarctica, dynamic discharge was accelerated from present-day net discharge (19) in the first decade and held thereafter to the highest outlet glacier velocity observed anywhere [14.6 km/year (6)], and Lambert/Amery was accelerated from present-day net discharge (19) in the first decade by an order of magnitude and held thereafter. Antarctic Peninsula and GIC were calculated by scaling dynamic discharge at the dynamics-to-SMB ratio computed for Greenland; this ratio is larger (6.42) than in case Low 1 because Greenland's dynamic discharge is larger. The net result, including thermal expansion, is 2008 mm by 2100 (Table 3).

On the basis of calculations presented here, we suggest that an improved estimate of the range of SLR to 2100 including increased ice dynamics lies between 0.8 and 2.0 m. We emphasize that assumptions made to arrive here contain substantial uncertainties, and many other scenarios and combinations of contributions could be considered. However, the net eustatic SLR from other combinations explored fell within the range given in Table 3. Hence, these values give a context and starting point for refinements in SLR forecasts on the basis of clearly defined assumptions and offer a more plausible range of estimates than those neglecting the dominant ice dynamics term. Certain potentially significant sinks and sources of SLR, such as terrestrial water storage, are still absent altogether. Among the uncertainties explored, the potential for dynamic response from GIC is comparable in magnitude to dynamic response from Greenland or Antarctica but is exceptionally poorly constrained by basic observations. Without better knowledge of the number, size, and catchment areas of marine-based outlet glaciers in the GIC category, improvements on the estimates made here will be very difficult.

References and Notes
1. S. O'Neel, W. T. Pfeffer, *Geophys. Res. Lett.* **34**, L22502 (2007).
2. M. F. Meier, A. Post, *J. Geophys. Res.* **92**, 9051 (1987).
3. M. Meier et al., *J. Geophys. Res.* **99**, 15219 (1994).
4. B. Kamb et al., *J. Geophys. Res.* **99**, 15231 (1994).
5. E. Rignot, P. Kanagaratnam, *Science* **311**, 986 (2006).
6. I. M. Howat, I. Joughin, T. A. Scambos, *Science* **315**, 1559 (2007); published online 7 February 2007 (10.1126/science.1138478).
7. I. Joughin, W. Abdalati, M. Fahnestock, *Nature* **432**, 608 (2004).
8. IPCC, *Climate Change 2007: The Physical Science Basis. Contribution of Working Group I to the Fourth Assessment Report of the Intergovernmental Panel on Climate Change,* S. Solomon et al., Eds. (Cambridge Univ. Press, Cambridge, 2007).

9. B. L. Otto-Bliesner et al., Science 311, 1751 (2006).
10. J. T. Overpeck et al., Science 311, 1747 (2006).
11. J. Hansen, Environ. Res. Lett. 2, 024002 (2007).
12. J. Hansen et al., Philos. Trans. R. Soc. London Ser. A 365, 1925 (2007).
13. J. Mount, R. Twiss, San Francisco Estuary Watershed Sci. 3, 1 (2005).
14. E. Bard et al., Nature 382, 241 (1996).
15. M. F. Meier et al., Science 317, 1064 (2007); published online 18 July 2007 (10.1126/science.1143906).
16. J. L. Bamber, R. L. Layberry, S. Gogineni, J. Geophys. Res. 106, 33773 (2001).
17. B. Kamb et al., Science 227, 469 (1985).
18. E. R. Hope, "English translation T409R," Defense Research Board, Ottawa, Canada, 1963 [translation from L. D. Dolgushin, S. A. Yevteyev, A. N. Krenke, K. P. Rototayev, N. M. Svatkov, Priroda 11, 84 (1963)].
19. E. Rignot et al., Nat. Geosci. 1, 106 (2008).
20. E. Rignot, personal communication (2007).
21. R. Thomas et al., Science 289, 426 (2000).
22. G. A. Meehl et al., in (8).
23. This work was supported by NSF grants OPP-0327345 and OPP-0622351, and a University of Colorado Faculty Fellowship (W.T.P.), NSF grants OPP-0612506 and

OPP-0454789 (J.T.H.), and the Greens Foundation at Scripps Institution of Oceanography (S.O.). E. Rignot generously supplied Greenland surface velocity data.

Apobec3 Encodes *Rfv3*, a Gene Influencing Neutralizing Antibody Control of Retrovirus Infection

Mario L. Santiago,[1] Mauricio Montano,[1]* Robert Benitez,[1]* Ronald J. Messer,[2] Wes Yonemoto,[1] Bruce Chesebro,[2] Kim J. Hasenkrug,[2]† Warner C. Greene[1,3,4]†

Recovery from Friend virus 3 (*Rfv3*) is a single autosomal gene encoding a resistance trait that influences retroviral neutralizing antibody responses and viremia. Despite extensive research for 30 years, the molecular identity of *Rfv3* has remained elusive. Here, we demonstrate that *Rfv3* is encoded by *Apobec3*. *Apobec3* maps to the same chromosome region as *Rfv3* and has broad inhibitory activity against retroviruses, including HIV. Not only did genetic inactivation of *Apobec3* convert *Rfv3*-resistant mice to a susceptible phenotype, but *Apobec3* was also found to be naturally disabled by aberrant messenger RNA splicing in *Rfv3*-susceptible strains. The link between *Apobec3* and neutralizing antibody responses highlights an *Apobec3*-dependent mechanism of host protection that might extend to HIV and other human retroviral infections.

The study of viral resistance factors has provided important insights into the evolutionary strategies of defense used by mammalian hosts (1–5). Recovery from Friend virus (FV) gene 3 (*Rfv3*) was first identified as a resistance trait in 1978 (6, 7), and later genetic studies showed that the phenotypes of decreased viremia and FV-specific neutralizing antibody responses segregated as a single gene (8). Because the generation of neutralizing antibodies is critical for recovery from FV infection (1, 9) and a desired but often unrealized outcome in various retroviral infections, including HIV-1, we

have focused our efforts on identifying the gene encoding *Rfv3*. The *Rfv3* locus maps to a 0.83-centimorgan region of chromosome 15 (fig. S1A) (10–12), which contains at least 61 annotated genes (table S1), one of which is murine *Apobec3* (mA3), a member of a family of deoxycytidine deaminases with antiretroviral and antiretroelement activity [as reviewed in (13)]. This fact, along with the presence of substantial polymorphism in mA3 (table S1), led us to consider mA3 as a prime candidate for *Rfv3*.

Because *Rfv3* has no described in vitro phenotype, our investigation required the generation

of mA3-deficient mice (14). First, an inactivated mA3 gene (fig. S1B) was introduced into the *Rfv3*$^{r/r}$ C57BL/6 (B6) background to test its ability to act as a defective *Rfv3* allele in matings with *Rfv3*$^{s/s}$ mice (table 1). Because the *Rfv3* resistance trait is dominant over susceptibility (7), *Rfv3*$^{s/s}$ F$_1$ offspring should control viremia and mount effective neutralizing antibody responses. Conversely, if mA3 encodes *Rfv3*, then the gene from a mA3$^{-/-}$ parent will be null, and the resultant F$_1$ offspring with an *Rfv3*$^{r/s}$ genotype are predicted to exhibit higher levels of viremia and weaker neutralizing antibody responses. To test this possibility, B6 x BALB/c F$_1$ offspring were infected with FV and plasma viremia levels were measured. At 7 days post infection (dpi), the F$_1$ mice containing an inactivated mA3 gene exhibited levels of viremia 15 times as high as their congenic partners carrying the wild-type mA3 allele (Fig. 1A). These high viral loads in mA3$^{-/-}$ F$_1$ mice were comparable to FV levels found in fully susceptible *Rfv3*$^{s/s}$ BALB/c parental mice. Thus, mA3 is a restriction factor contributing to the

[1]Gladstone Institute of Virology and Immunology, San Francisco, CA 94158, USA. [2]Laboratory of Persistent Viral Diseases, Rocky Mountain Laboratories, National Institute of Allergy and Infectious Diseases, Hamilton, MT 59840, USA. [3]Department of Medicine, University of California, San Francisco, CA 94143–1230, USA. [4]Department of Microbiology and Immunology, University of California, San Francisco, CA 94143–1230, USA.

*These authors contributed equally to this work.
†To whom correspondence should be addressed. E-mail: khasenkrug@nih.gov (K.J.H.); wgreene@gladstone.ucsf.edu (W.C.G.)

Table 1. FV infection characteristics of various mouse strains used in this study.

Type	Strain	General FV susceptibility	Viremia	*Rfv3*	Neutralizing antibody	*H-2**	Cell-mediated immunity	*Fv2*†	Splenomegaly induction
Wild-type	C57BL/6 (B6)	Resistant	Resistant	r/r	High	b/b	High	r/r	No
	BALB/c	Susceptible	Chronic	s/s	Low	d/d	Very low	s/s	Yes
	A.BY	Susceptible	Chronic	s/s	Low	b/b	High	s/s	Yes
	129/Ola‡	Resistant	Resistant	r/r	High	b/b	High	r/r	No
F$_1$ hybrids	B6 x BALB/c	Susceptible	Acute	r/s	High	b/d	Low	r/s	Yes
	B6 x A.BY	Susceptible	Acute	r/s	High	b/b	High	r/s	Yes

*H-2 is the murine major histocompatibility complex that dictates cell-mediated immunity against FV (5, 15). †Fv2 is a dominant FV susceptibility gene that facilitates splenomegaly induction through aberrant signaling in erythroblasts (4). ‡FV susceptibility data on 129/Ola were based on results from this study (Fig. 2O (14). The cell-mediated immune response of this strain was inferred from its H-2 haplotype.

early control of FV infection in adult immuno-competent mice.

Rfv3-mediated recovery from FV infection correlates strongly with FV-specific neutralizing antibody responses at 28 dpi (7). Thus, *mA3*+ and *mA3* F$_1$ congenic strains were monitored for up to 1 month after FV infection. However, F$_1$ mice lacking the B6 *mA3* allele suffered a markedly higher rate of FV-induced death (Fig. 1B), indicating that, like *Rfv3*+ susceptibility, *mA3* inactivation compromised recovery from FV disease. Compared with *mA3*+ F$_1$ mice, the three surviving *mA3* F$_1$ mice exhibited mean viremia higher by a factor of 14 (fig. S2A) and low FV-specific neutralizing antibody titers at 28 dpi (fig. S2B), but the small number of surviving animals precluded obtaining statistically significant data. Therefore, separate cohorts of mice were studied for FV-specific antibodies at 14 dpi, before the steep decline in survival of *mA3* F$_1$ mice. The *mA3* F$_1$ mice exhibited significantly less FV binding antibody than *mA3*+ F$_1$ mice, and the low levels of FV antibodies in *mA3* F$_1$ mice proved comparable to levels detected in the parental *Rfv3*s/s BALB/c mice (Fig. 1C). These findings indicated that *mA3* influenced FV-specific antibody responses.

To better assess FV-specific neutralizing antibody responses in mice expressing or lacking *mA3*, these studies were repeated in high-recovery B6 x A.BY F$_1$ mice, which generally survive more than 1 month after FV infection because of protective cell-mediated immune responses associated with the *H-2*b/b haplotype (Table 1) (5, 15). Plasma samples obtained at 28 dpi revealed significantly lower FV-specific neutralizing antibody titers in *mA3* F$_1$ mice

compared with *mA3*+ F$_1$ mice (Fig. 1D). These findings confirmed that *mA3* influenced FV-specific neutralizing antibody responses and demonstrated that this effect operated independently of *H-2*, a known property of *Rfv3* (7).

Purebred B6 mice are highly resistant to FV infection (Table 1), but their resistance can be overcome by inoculating aged mice with high doses of FV (16) or by using immunodeficient mice, including those that fail to produce specific antibodies (9). Genetic inactivation of *mA3* in B6 mice might therefore recapitulate the *Rfv3*s susceptible phenotype without a requirement for outcrossing to susceptible strains. To test this possibility, >16-week-old B6 *mA3*+/+ and *mA3*−/− mice were infected with FV. Plasma viremia was 6.2 times as high in *mA3*−/− mice as in *mA3*+/+ mice at 8 dpi (Fig. 2A). Furthermore, *mA3*−/− mice exhibited significantly lower neutralizing antibody titers than wild-type mice by 28 dpi (Fig. 2B). Thus, *mA3* inactivation was sufficient both to enhance viremia and to diminish neutralizing antibody production even in the highly resistant B6 genetic background. These results were confirmed in a second highly resistant strain of mice, 129/Ola (Table 1 and Fig. 2C) (14). Together, these findings demonstrate that genetic inactivation of *mA3* recapitulates the *Rfv3*s phenotype and indicate that *Rfv3* is encoded by *mA3*.

Both resistant and susceptible mouse strains contain the *mA3* gene and express *mA3* mRNA. Cloning of splenocyte *mA3* mRNA from the *Rfv3*r/r 129/Ola strain revealed the predominant expression of a full-length *mA3* transcript, whereas most mRNA transcripts from *Rfv3*s/s B6 mice lacked exon 5 sequences (figs. S3 and S4) (17).

mA3 transcripts from both *Rfv3*s/s strains BALB/c and A.BY were distinguished by the absence of exon 2 sequences (Fig. 3A and fig. S4). Quantitative reverse transcription polymerase chain reaction (RT-PCR) revealed similar levels of total *mA3* mRNA in both the *Rfv3*s/s and *Rfv3*s/s strains but a lower level by a factor of 17 of Exon2-containing transcripts in both *Rfv3*s/s mouse strains (Fig. 3B). Thus, the presence of an alternatively spliced *mA3* mRNA lacking exon 2 correlated with the *Rfv3*s-susceptible phenotype.

Translational read-through of the *mA3* mRNA lacking exon 2 predicts two possible outcomes: no mA3 protein expression or a truncated mA3 protein (Fig. 3A and fig. S5). Without suitable mA3 antibodies, these outcomes cannot be distinguished. We investigated the antiviral activity of this latter Δexon 2 mA3 protein by cloning it as a fusion with an N-terminal triple FLAG epitope tag. NIH3T3 cells were cotransfected with the expression construct and an FV molecular clone (pLRB302) (18) to test the infectivity of the resulting FV virions. For comparison, cotransfections were performed with a FLAG-tagged expression construct containing the *mA3* cDNA with exon 5. When standardized for relative mA3 expression levels, the BALB/c Δexon 2 mA3 protein was at least 3 to 5 times less potent at inhibiting FV infectivity than was the B6 Δexon 5 mA3 protein (Fig. 3C). In control experiments, the full-length mA3 protein from 129/Ola also potently inhibited FV (fig. S6). These data indicated that, even if a truncated mA3 protein were expressed in *Rfv3*s/s mice, its antiviral activity would be significantly impaired.
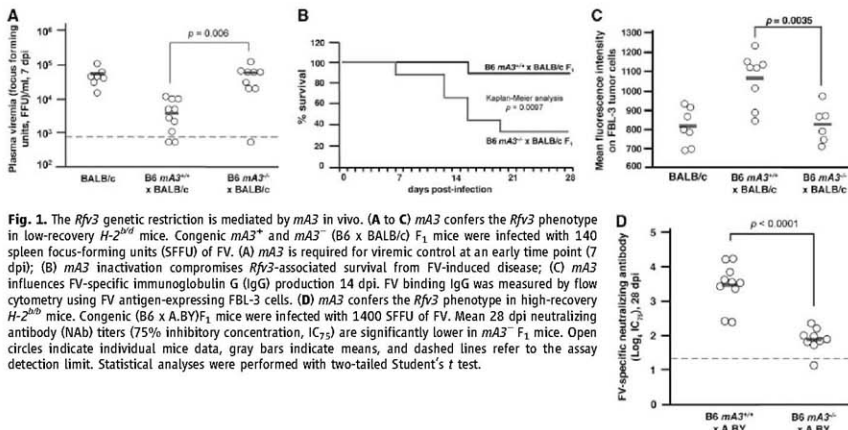

Fig. 1. The *Rfv3* genetic restriction is mediated by *mA3* in vivo. (**A to C**) *mA3* confers the *Rfv3* phenotype in low-recovery *H-2*b/d mice. Congenic *mA3*+ and *mA3*− (B6 x BALB/c) F$_1$ mice were infected with 140 spleen focus-forming units (SFFU) of FV. (A) *mA3* is required for viremic control at an early time point (7 dpi); (B) *mA3* inactivation compromises *Rfv3*-associated survival from FV-induced disease; (C) *mA3* influences FV-specific immunoglobulin G (IgG) production 14 dpi. FV binding IgG was measured by flow cytometry using FV antigen-expressing FBL-3 cells. (**D**) *mA3* confers the *Rfv3* phenotype in high-recovery *H-2*b/b mice. Congenic (B6 x A.BY)F$_1$ mice were infected with 1400 SFFU of FV. Mean 28 dpi neutralizing antibody (NAb) titers (75% inhibitory concentration, IC$_{75}$) are significantly lower in *mA3* F$_1$ mice. Open circles indicate individual mice data, gray bars indicate means, and dashed lines refer to the assay detection limit. Statistical analyses were performed with two-tailed Student's *t* test.

The involvement of *mA3* in the control of FV viremia before the onset of adaptive anti-FV immune responses confirms its stature as a bona fide innate immune factor in vivo. In addition, *mA3* influences the development of virus-specific neutralizing antibody responses, perhaps by (i) limiting the early viral antigenic load and evading a form of "high-zone tolerance" (*19–21*) or (ii) inhibiting early FV-induced injury of critical cell types, such as B cells, T cells, or antigen-presenting cells, required for the development of FV-specific humoral immunity. However, mA3 is expressed in B cells and is evolutionarily related to activation-induced deaminase, an enzyme that controls somatic hypermutation and class-switch recombination in these cells (*22*). Thus, mA3 may conceivably be involved in shaping the antibody repertoire.

The human *Apobec3* family has been implicated in the control of HIV-1 infection, but HIV-1 encodes Vif, which thwarts the actions of Apobec3G (A3G) and Apobec3F (A3F) (*23–26*). Compromised A3G/A3F antiviral activity may therefore contribute to the generally poor neutralizing antibody response observed in HIV-1 infection (*27*). Vif antagonists, if and when they are available, may enhance the generation of effective humoral immune responses against HIV-1. Finally, studies exploring the apparent intrinsic resistance of individuals who are extensively exposed to HIV-1, yet remain uninfected, have genetically mapped this phenotype to chromosome 22q12-13 (*12*), a location distinguished by a tandem array of the seven human *Apobec3* family members. Genome-wide studies of the entire human *Apobec3* locus, with particular emphasis on functional differences induced by alternative splicing, are clearly merited to fully explore the potential contribution of this gene family to HIV resistance, neutralizing antibody production, and disease progression.

Fig. 2. *mA3* influences FV-specific neutralizing antibody responses in highly resistant (*Fv2$^{r/r}$*) mice. (**A** and **B**) *mA3$^{+/+}$* and *mA3$^{-/-}$* B6 mice (>16 weeks old) were infected with 5000 SFFU of FV. (A) *mA3* influences early viremic control at 8 dpi; (B) *mA3* is required for FV-specific neutralizing antibody production 28 dpi. (**C**) *mA3* influences neutralizing antibody responses in 129/Ola mice. *mA3$^{+/+}$* and *mA3$^{-/-}$* 129/Ola mice were crossed with *mA3$^{+/+}$* and *mA3$^{-/-}$* B6 mice to generate F$_1$ offspring. FV-specific neutralizing antibody titers (IC$_{75}$) at 28 dpi with 5000 SFFU of FV are shown. Additional information is found in SOM text and (*14*). Statistical analysis was performed using a two-tailed Student's *t* test.

Fig. 3. Molecular basis of *Rfv3^s* susceptibility. (**A**) Aberrant *mA3* exon 2 splicing in *Rfv3$^{s/s}$* mice. If the wild-type mA3 open reading frame (ORF1) is used, frameshift-induced translational termination will result in a nonfunctional peptide. However, two start sites in an alternative reading frame (ORF3) may be used to translate a mutant mA3 protein with a novel N terminus and a 56 amino acid deletion. (**B**) Decreased Exon2$^+$, but not total *mA3* transcripts, in *Rfv3$^{s/s}$* mice. Quantitative RT-PCR of total (left) and Exon2$^+$ (right) *mA3* splenocyte transcripts in *Rfv3$^{r/r}$* and *Rfv3$^{s/s}$* mouse strains was performed. Amplification levels were normalized to beta-actin (left) or total *mA3* (right). (**C**) Decreased antiviral activity of the mA3 Δexon2 relative to the mA3 Δexon5 spliceoform. An FV molecular clone was cotransfected in NIH3T3 cells with FLAG-tagged mA3 constructs. The infectivity of harvested virions was assayed in *Mus dunni* cells and normalized against reverse transcriptase activity. Cotransfections with FLAG vector alone were set at 0% inhibition. Expression of mA3 was assessed by anti-FLAG immunoblotting. Error bars correspond to SD from triplicate experiments.

References and Notes

1. K. J. Hasenkrug, B. Chesebro, *Proc. Natl. Acad. Sci. U.S.A.* **94**, 7811 (1997).
2. W. Li, W. R. Green, *J. Virol.* **80**, 5777 (2006).
3. S. Best, P. Le Tissier, G. Towers, J. P. Stoye, *Nature* **382**, 826 (1996).
4. D. A. Persons *et al.*, *Nat. Genet.* **23**, 159 (1999).
5. W. J. Britt, B. Chesebro, *J. Exp. Med.* **157**, 1736 (1983).
6. B. Chesebro, K. Wehrly, in *Advances in Comparative Leukemia Research*, P. Bentvelzen, Ed. (North-Holland Biomedical Press, Elsevier, 1978), pp. 69–73.
7. B. Chesebro, K. Wehrly, *Proc. Natl. Acad. Sci. U.S.A.* **76**, 425 (1979).
8. B. Doig, B. Chesebro, *J. Exp. Med.* **150**, 10 (1979).
9. K. J. Hasenkrug, *J. Virol.* **73**, 6468 (1999).
10. K. J. Hasenkrug *et al.*, *J. Virol.* **69**, 2617 (1995).
11. H. J. Super *et al.*, *J. Virol.* **73**, 7848 (1999).
12. Y. Kanari *et al.*, *AIDS* **19**, 1015 (2005).
13. Y. L. Chiu, W. C. Greene, *Annu. Rev. Immunol.* **26**, 317 (2008).
14. Materials and methods are available as supporting material on *Science* Online.
15. B. Chesebro, K. Wehrly, *J. Exp. Med.* **143**, 73 (1976).
16. H. C. Van der Gaag, A. A. Axelrad, *Virology* **177**, 837 (1990).
17. S. J. Rulli Jr. *et al.*, *J. Virol.* **82**, 6566 (2008).
18. J. L. Portis, F. J. McAtee, S. C. Kayman, *J. Acquir. Immune Defic. Syndr.* **5**, 1272 (1992).
19. J. G. Monroe, A. Lowy, R. D. Granstein, M. I. Greene, *Immunol. Rev.* **80**, 103 (1984).
20. A. Gonzalez-Fernandez, C. Milstein, *Immunology* **93**, 149 (1998).
21. Y. T. Kim, G. W. Siskind, *Clin. Exp. Immunol.* **17**, 329 (1974).
22. M. Muramatsu *et al.*, *Cell* **102**, 553 (2000).
23. K. Stopak, C. de Noronha, W. Yonemoto, W. C. Greene, *Mol. Cell* **12**, 591 (2003).
24. M. Marin, K. M. Rose, S. L. Kozak, D. Kabat, *Nat. Med.* **9**, 1398 (2003).
25. A. M. Sheehy, N. C. Gaddis, M. H. Malim, *Nat. Med.* **9**, 1404 (2003).
26. Y. H. Zheng *et al.*, *J. Virol.* **78**, 6073 (2004).
27. D. R. Burton *et al.*, *Nat. Immunol.* **5**, 233 (2004).
28. We thank the Transgenic Core Laboratory, the Animal Facility, and S. Espineda at the J. David Gladstone Institutes for technical assistance; L. Evans, J. Portis, R. Gallo, R. Locksley, and members of the Greene and Hasenkrug Laboratory for helpful discussions; and R. Givens, S. Cammack, and G. Howard for manuscript preparation. This work was supported by the NIAID Division of Intramural Research at NIH to K.J.H. and B.C., an NIH R01 AI065329 to W.C.G., and an NIH facility grant to the J. David Gladstone Institutes. Sequences are deposited in GenBank, with accession numbers EU707568 to EU707571.

Human-Specific Gain of Function in a Developmental Enhancer

Shyam Prabhakar,[1]* Axel Visel,[1] Jennifer A. Akiyama,[1] Malak Shoukry,[1] Keith D. Lewis,[1]† Amy Holt,[1] Ingrid Plajzer-Frick,[1] Harris Morrison,[2] David R. FitzPatrick,[2] Veena Afzal,[1] Len A. Pennacchio,[1,3] Edward M. Rubin,[1,3]‡ James P. Noonan[1]§

Changes in gene regulation are thought to have contributed to the evolution of human development. However, in vivo evidence for uniquely human developmental regulatory function has remained elusive. In transgenic mice, a conserved noncoding sequence (*HACNS1*) that evolved extremely rapidly in humans acted as an enhancer of gene expression that has gained a strong limb expression domain relative to the orthologous elements from chimpanzee and rhesus macaque. This gain of function was consistent across two developmental stages in the mouse and included the presumptive anterior wrist and proximal thumb. In vivo analyses with synthetic enhancers, in which human-specific substitutions were introduced into the chimpanzee enhancer sequence or reverted to the human enhancer to the ancestral state, indicated that 13 substitutions clustered in an 81–base pair module otherwise highly constrained among terrestrial vertebrates were sufficient to confer the human-specific limb expression domain.

Genome sequence changes that altered the molecular machinery of development likely facilitated the evolution of uniquely human morphological traits (*1*, *2*). Although these genetic modifications remain largely unidentified, it has long been thought that they included changes in gene expression due to positive selection for nucleotide substitutions that altered the activity of cis-regulatory elements (*3*). Several cases of putatively adaptive sequence change, including polymorphisms among human populations

and apparently fixed differences between humans and other primates, have been shown to affect in vitro promoter or enhancer function in cell line reporter assays (*4*–*7*). However, the impact of human-specific nucleotide substitutions on the in vivo activity of developmental regulatory elements remains obscure.

In vivo analyses of evolutionarily conserved noncoding sequences have revealed them to be enriched in cis-regulatory transcriptional enhancers that confer specific expression patterns during development (*8*–*11*). Recent efforts have identified conserved noncoding sequences that evolved rapidly in the human lineage, but it is not known whether these sequences include regulatory elements with altered activities in humans (*12*–*15*). Here, we focus on functionally characterizing the most rapidly evolving human noncoding element yet identified, which we termed human-accelerated conserved noncoding sequence 1 (*HACNS1*) (*12*). Although this 546–base pair (bp) element is highly constrained in all sequenced terrestrial vertebrate genomes, it has accumulated 16 human-specific

sequence changes in the ~6 million years since the human-chimpanzee split (Fig. 1A). We evaluated the significance of this evolutionary acceleration by means of a test statistic that represents the log-likelihood, or information theoretic "surprisal," of observing the human sequence given the orthologous sequences from multiple terrestrial vertebrates. Assuming *HACNS1* is under functional constraint in humans, its rapid divergence is highly unexpected given its strong conservation in these other species [surprisal test P value = 9.2×10^{-12} (*16*)]. This divergence also significantly exceeds the ~4 substitutions expected if *HACNS1* were evolving at the neutral substitution rate in humans [surprisal test P value = 1.3×10^{-6} (*16*)]. One explanation for this marked acceleration is that *HACNS1* has undergone several instances of positive selection during human evolution that may have altered its function.

To test this hypothesis, we evaluated the ability of *HACNS1* and its orthologs from chimpanzee and rhesus macaque to function as transcriptional enhancers during development, using a transgenic mouse enhancer assay in which the activity of each sequence is assessed through a β-galactosidase (*lacZ*) reporter gene coupled to a minimal *Hsp68* promoter (*17*). We initially examined the potential enhancer activity of *HACNS1* at embryonic day 11.5 (E11.5). We tested a 1.2-kb DNA fragment encompassing *HACNS1* that also contained nonconserved sequences flanking the element, in order to include possible functional sequences near *HACNS1* not detected by conservation (table S1). At E11.5, the human element drove strong and reproducible reporter gene expression in the anterior limb bud, pharyngeal arches, and developing ear and eye, which suggests that *HACNS1* acts as a robust enhancer during development (Fig. 1, B and C, and fig. S1). In striking contrast to the highly reproducible staining driven by the human enhancer, which extended into the most distal region of the anterior limb bud in five of six lacZ-positive embryos (Fig. 1C and *HACNS1* embryos

[1]Genomics Division, Lawrence Berkeley National Laboratory, Berkeley, CA 94720, USA. [2]MRC Human Genetics Unit, Western General Hospital, Edinburgh EH4 2XU, UK. [3]United States Department of Energy Joint Genome Institute, Walnut Creek, CA 94598, USA.

*Present address: Computational and Mathematical Biology, Genome Institute of Singapore 138672, Singapore.
†Present address: Division of Biology, California Institute of Technology, Pasadena, CA 91125, USA.
‡To whom correspondence should be addressed. E-mail: emrubin@lbl.gov (E.M.R.); james.noonan@yale.edu (J.P.N.)
§Present address: Department of Genetics, Yale University School of Medicine, New Haven, CT 06520, USA.

1 to 5 in fig. S1), the chimpanzee and rhesus orthologs failed to drive reproducible reporter gene expression in the distal limb bud, although they did drive moderately reproducible expression at the base of the limb (Fig. 1, B and C; chimpanzee enhancer embryos 1, 2, 6, 7, and 8 and rhesus enhancer embryos 1 to 4, 6 to 8, and 10 in fig. S1).

Two of the embryos that were transgenic for the chimpanzee ortholog showed this pattern also exhibited diffuse, low-level staining that extended into the anterior limb, which suggests that the chimpanzee enhancer may possess a weak capacity to drive expression in this structure (embryos 4 and 7 in fig. S1). However, this infrequent pattern was in stark contrast to the strong and highly reproducible pattern of the human enhancer. Furthermore, pharyngeal arch, eye, and ear expression was less reproducible and, where present, generally weaker in multiple positive embryos for both nonhuman orthologs; these findings suggest additional sites of reduced overall enhancer activity relative to the human ortholog.

To assess the HACNS1 limb expression pattern at higher resolution, we sectioned HACNS1 transgenic embryos and found that staining in the forelimb was restricted to the mesenchyme, forming a continuous expression domain that extended deep into the limb bud along the anteroposterior axis at the handplate and shoulder while remaining more anterior in between (fig. S3). These results provide evidence that the human-specific sequence changes in HACNS1 have resulted in a gain of function in this otherwise highly conserved enhancer, increasing its overall robustness and producing a strong human-specific expression domain in the anterior limb bud mesenchyme at E11.5. Because the chimpanzee and rhesus orthologs yield similar patterns to each other and show consistent differences relative to HACNS1, a parsimonious conclusion would be that the chimpanzee and rhesus patterns reflect the ancestral primate state from which the human-specific pattern has evolved.

To explore the activity of HACNS1 at a more advanced stage of limb development, we compared the expression patterns of the human, chimpanzee, and rhesus enhancers in E13.5 transgenic mouse embryos. At this stage, the human element continued to drive reproducible reporter gene expression in the anterior developing forelimb, particularly in the shoulder and the anterior junction of the forearm and handplate, in 11 of 12 positive embryos (Fig. 2, A to C; embryos 1 to 10 and 12 in fig. S2). In four of these embryos, the reporter gene activity extended into the future anterior-most digit of the forelimb (Fig. 2B). Simi-lar expression, although with weaker staining, was also observed in the corresponding structures in the hindlimb. Imaging of lacZ staining in a representative HACNS1 transgenic embryo by means of optical projection tomography [OPT (18)] revealed that the anterior expression evident in the whole mount extended deep inside the limb at the forearm-handplate junction (fig. S4). The orthologous chimpanzee and rhesus elements failed to drive reproducible expression in the distal limbs at this time point, although a subset of positive embryos in each case (4 of 10 for chimpanzee; 3 of 12 for rhesus) showed reporter gene expression in the shoulder region of the limb bud, thus recapitulating the proximal tip of the expression domain of the human enhancer (Fig. 2A; chimpanzee enhancer embryos 2 to 5 and rhesus enhancer embryos 1, 5, and 6 in fig. S2). OPT imaging confirmed the absence of reproducible lacZ staining inside the distal limb in representative embryos transgenic for the rhesus and chimpanzee enhancers (fig. S4). These results indicate that the human-specific enhancer activity persists across multiple developmental stages. Moreover, they suggest that the robust anterior limb expression pattern of HACNS1 evolved from a weaker ancestral pattern that is largely confined to the base of the limb bud, as evident in the
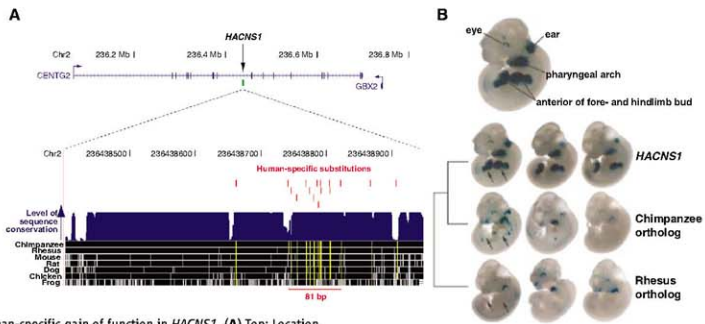

Fig. 1. Human-specific gain of function in *HACNS1*. (**A**) Top: Location of *HACNS1* in NCBI build 36.1 of the human genome assembly. Bottom: Sequence alignment of *HACNS1* with orthologs from other vertebrate genomes; positions identical to human are shown in black. A quantitative plot of sequence conservation is shown in blue above the alignment (26–28). The location of each human-specific substitution is indicated by a vertical red line, and the depth of nonhuman evolutionary conservation at human-substituted positions is shown by a vertical yellow line that indicates whether each sequence is identical to chimpanzee and rhesus at that position. The cluster of 13 human-specific substitutions in 81 bp is also indicated. (**B**) Expression patterns obtained from the *HACNS1* enhancer and orthologous sequences from chimpanzee and rhesus driving expression of a *lacZ* reporter gene in E11.5 mouse embryos. Arrows indicate positions in the anterior limb bud where reproducible reporter gene expression is present or absent. A representative *HACNS1* embryo is shown at top to illustrate the relevant anatomical structures. Three embryos resulting from independent transgene integration events are shown for each orthologous sequence tested. (**C**) Number of embryos transgenic for each sequence displaying the limb expression patterns described in the text.
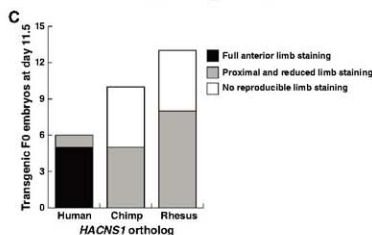
activities of the chimpanzee and rhesus enhancers at both time points.

We next sought to identify human-specific sequence changes responsible for the functional change in the human enhancer. Although the 16 human-specific substitutions within the 546-bp conserved region corresponding to *HACNS1* are the most striking feature of the 1.2-kb orthologous segments we initially tested for enhancer function, these segments also included ~650 bp of nonconserved DNA containing additional human-chimpanzee sequence differences. To isolate the effect of the substitutions within *HACNS1* on enhancer function, we synthesized a chimeric 1.2-kb enhancer in which we transferred all 16 substitutions into the chimpanzee sequence background (*16*). This "humanized" chimpanzee enhancer produced an E11.5 expression pattern nearly identical to that of the native human enhancer; this finding suggests that the human-specific sequence changes within *HACNS1* are responsible for the gain of function we observed (8 of 8 embryos; Fig. 3D and fig. S1). Strikingly, these human-specific substitutions were significantly clustered: 13 of 16 substitutions occurred within an 81-bp region of the 546-bp conserved element [permutation test P value = 1.7×10^{-7} (*16*)], which suggests that this region may be particularly relevant to the human-specific function of *HACNS1* (Figs. 1A and 3A).

To test this hypothesis, we synthesized a chimeric 1.2-kb enhancer in which the 13 clustered human substitutions were introduced into the chimpanzee sequence background (table S2).

At E11.5, this element produced an anterior limb bud pattern highly similar to the *HACNS1* pattern (6 of 6 positive embryos; Fig. 3 and fig. S1). We also performed the reciprocal experiment, synthesizing a complementary chimeric enhancer where we replaced the 13 human-specific nucleotides in the human enhancer sequence with their putatively ancestral orthologs from chimpanzee. This "reverted" enhancer yielded a pattern very similar to the chimpanzee and rhesus enhancer patterns shown in Fig. 1B, with expression in the anterior limb bud greatly reduced or absent (Fig. 3 and fig. S1). These results confirm the robustness of the functional differences we observed between *HACNS1* and its chimpanzee and rhesus orthologs, and they indicate that the *HACNS1* anterior limb bud pattern is largely attributable to one or more of the 13 clustered human-specific substitutions we identified. To further dissect the functional contribution of these substitutions, we introduced independent groups of six substitutions and three substitutions into the chimpanzee enhancer sequence (fig. S5). These enhancers drove variable expression in the anterior limb bud, which suggests that at least two human-specific substitutions are required for the gain of function in *HACNS1*.

The precise molecular mechanism by which the substitutions in *HACNS1* confer the human-specific expression pattern remains to be determined. Computational analysis of predicted transcription factor binding sites in *HACNS1* and its nonhuman orthologs suggested that multiple sites have been gained and lost in this enhancer

during human evolution (fig. S6). Predicted human-specific binding sites for the developmental transcription factors PAX9 and ZNF423 may contribute to *HACNS1* enhancer activity, given that the known expression pattern of *PAX9* in the mouse limb overlaps the human-specific limb domain of *HACNS1* at E11.5 and E13.5, and *ZNF423* is expressed in the mouse handplate mesenchyme from E10.5 through E12.5 (*19–21*).

Multiple lines of evidence suggest that the functional changes in *HACNS1* are due to adaptive evolution. The rate of human-specific accelerated evolution in *HACNS1* is more than 4 times the local neutral rate. Moreover, this rapid evolution cannot be explained purely on the basis of biased gene conversion (BGC), a neutral mechanism postulated to cause hotspots of accelerated evolution in the genome by increasing the local fixation rate of AT → GC substitutions (*22, 23*). Under the neutral BGC hypothesis, one would expect an increase in the overall substitution rate across the entire region of increased AT → GC substitution (*23*). An excess of AT → GC substitutions is indeed present in *HACNS1* [binomial test P value = 1.1×10^{-4} (*16*)], and the element lies in a ~5-kb genomic region enriched in such substitutions (Fig. 4). However, the human-specific substitution rate is elevated only in the narrow 81-bp region in *HACNS1* described above and is close to the local average outside of this window (Fig. 4). These data, coupled with the human-specific functional changes in *HACNS1*, argue against a purely neutral explanation for the rapid evolution of this element in humans.

Fig. 2. Gain of function in *HACNS1* persists at E13.5. (**A**) Expression patterns obtained from *HACNS1* and its chimpanzee ortholog in E13.5 mouse embryos. Three embryos resulting from independent transgene integration events are shown for each construct. Close-up views of forelimb and hindlimb expression in a representative embryo for each construct are shown at left, and arrows indicate positions where limb expression is present or absent. (**B**) Dorsal view of reporter gene expression in the distal anterior forelimb of a *HACNS1* E13.5 transgenic embryo. Arrow indicates the most anterior digit. (**C**) Number of embryos transgenic for each construct that display the limb expression patterns described in the text.
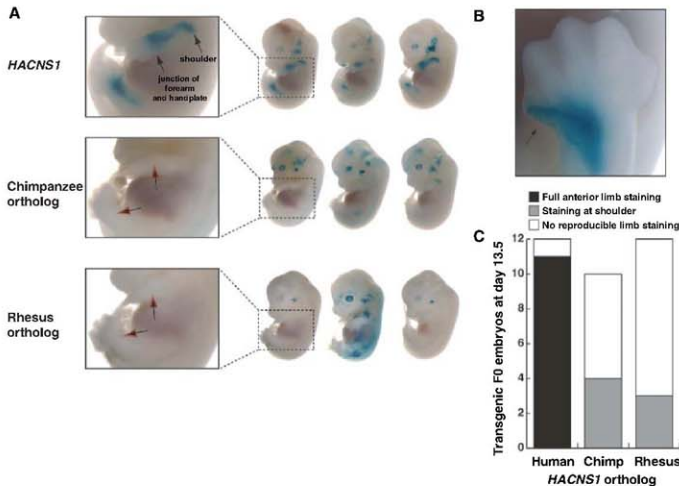
Our results evoke the hypothesis that human-specific adaptive evolution in *HACNS1* has contributed to uniquely human aspects of digit and limb patterning. The dexterity of the human hand is due to morphological differences compared with other primates that include rotation of the thumb toward the palm and an increase in the length of the thumb relative to the other digits (*1*). Human-specific changes in hindlimb morphology, such as the characteristic inflexibility and shortened digits of the human foot, facilitated habitual bipedalism. The gain of function in *HACNS1* may have influenced the evolution of these or other human limb features by altering the expression of nearby genes during limb development. *HACNS1* is located within an intron of *CENTG2*, which encodes a guanosine triphosphatase activating protein involved in the

regulation of endosome function. The next-closest gene is *GBX2*, which is located ~300 kb downstream of *HACNS1* and encodes an essential developmental transcription factor (*24, 25*). The role of *CENTG2* in limb development has not been evaluated. Mouse *Gbx2* is expressed in the developing limb, but *Gbx2* null mice have not been described as showing abnormal limbs (*25*). The potential impact of human-specific changes in the expression of these genes on limb development thus remains to be explored. We also note that the *HACNS1* expression pattern in transgenic mice may not entirely recapitulate the precise *HACNS1* expression pattern in the human embryo. We therefore cannot rule out the possibility that the accelerated evolution of *HACNS1* reflects selection for changes in structures other than, or in addition to, the limb. Elucidating the role of *HACNS1* in human morphological evolution requires further lines of evidence, including the analysis of *GBX2* and *CENTG2* expression during limb development and the generation of *HACNS1* targeted replacement mice. Independent of these considerations, our study suggests that adaptive nucleotide substitution altered the function of a developmental enhancer in humans, and illustrates a strategy that could be used across the genome to understand at a molecular level how human development evolved through cis-regulatory change.
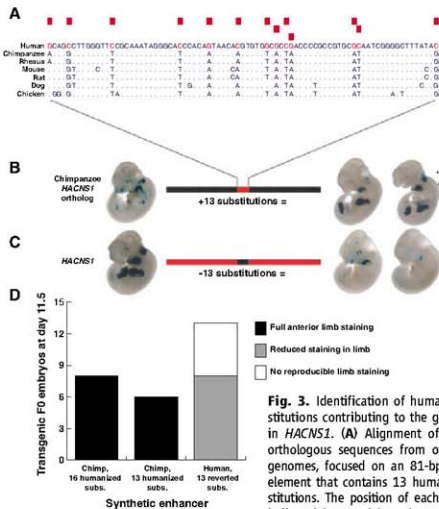
Fig. 3. Identification of human-specific substitutions contributing to the gain of function in *HACNS1*. (**A**) Alignment of *HACNS1* with orthologous sequences from other vertebrate genomes, focused on an 81-bp region in the element that contains 13 human-specific substitutions. The position of each substitution is indicated by a red box above the alignment; each human-specific nucleotide is highlighted in red. Positions in the nonhuman genomes that are identical to the human sequence are displayed as dots. (**B**) Expression pattern of a synthetic enhancer in which the 13 human-specific substitutions (red box) are introduced into the orthologous 1.2-kb chimpanzee sequence background (black bar). (**C**) Expression pattern of a synthetic enhancer obtained by reversion of these substitutions (black box) in the human sequence (red bar) to the nucleotide states in chimpanzee and rhesus. (**D**) Number of embryos transgenic for each synthetic enhancer that show full, partial, or no expression in the limb at E11.5.

Fig. 4. Human-specific substitution rate and proportion of AT → GC substitutions in *HACNS1* and flanking genomic region. The rate of human-specific substitutions (solid red line) and the fraction of human substitutions that are AT → GC events (solid blue line) were estimated in sliding windows across a 9-kb interval around *HACNS1*. The average values of each metric for 1 Mb of genomic sequence centered on *HACNS1* are shown for reference (dashed lines). The 546-bp interval corresponding to *HACNS1* is highlighted in yellow.
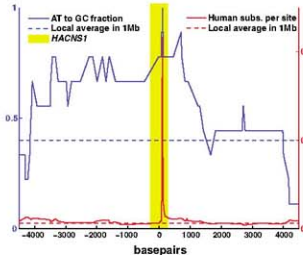
References and Notes

1. E. Trinkaus, in *The Cambridge Encyclopedia of Human Evolution*, S. Jones, R. Martin, D. Pilbeam, Eds. (Cambridge Univ. Press, New York, 1993), pp. 346–349.
2. S. B. Carroll, *Nature* **422**, 849 (2003).
3. M. C. King, A. C. Wilson, *Science* **188**, 107 (1975).
4. C. Toumamille *et al.*, *Nat. Genet.* **10**, 224 (1995).
5. M. V. Rockman *et al.*, *PLoS Biol.* **3**, e387 (2005).
6. S. A. Tishkoff *et al.*, *Nat. Genet.* **39**, 31 (2007).
7. G. A. Wray, *Nat. Rev. Genet.* **8**, 206 (2007).
8. D. Boffelli, M. A. Nobrega, E. M. Rubin, *Nat. Rev. Genet.* **5**, 456 (2004).
9. M. A. Nobrega, I. Ovcharenko, V. Afzal, E. M. Rubin, *Science* **302**, 413 (2003).
10. L. A. Pennacchio *et al.*, *Nature* **444**, 499 (2006).
11. A. Visel *et al.*, *Nat. Genet.* **40**, 158 (2008).
12. S. Prabhakar, J. P. Noonan, S. Pääbo, E. M. Rubin, *Science* **314**, 786 (2006).
13. K. S. Pollard *et al.*, *Nature* **443**, 167 (2006).
14. C. P. Bird *et al.*, *Genome Biol.* **8**, R118 (2007).
15. E. C. Bush, B. T. Lahn, *BMC Evol. Biol.* **8**, 17 (2008).
16. See supporting material on *Science* Online.
17. R. Kothary *et al.*, *Development* **105**, 707 (1989).
18. J. Sharpe *et al.*, *Science* **296**, 541 (2002).
19. A. Neubüser, H. Koseki, R. Balling, *Dev. Biol.* **170**, 701 (1995).
20. H. Peters, A. Neubüser, K. Kratochwil, R. Balling, *Genes Dev.* **12**, 2735 (1998).
21. S. Warming, T. Suzuki, T. P. Yamaguchi, N. A. Jenkins, N. G. Copeland, *Oncogene* **23**, 2727 (2004).
22. K. S. Pollard *et al.*, *PLoS Genet.* **2**, e168 (2006).
23. N. Galtier, L. Duret, *Trends Genet.* **23**, 273 (2007).
24. Z. Nie *et al.*, *J. Biol. Chem.* **277**, 48965 (2002).
25. K. M. Wassarman *et al.*, *Development* **124**, 2923 (1997).
26. M. Blanchette *et al.*, *Genome Res.* **14**, 708 (2004).
27. A. Siepel *et al.*, *Genome Res.* **15**, 1034 (2005).
28. W. J. Kent *et al.*, *Genome Res.* **12**, 996 (2002).
29. We thank members of the Pennacchio and Rubin laboratories for critical comments on the manuscript. Research was done under Department of Energy Contract

Wnt3a-Mediated Formation of Phosphatidylinositol 4,5-Bisphosphate Regulates LRP6 Phosphorylation

Weijun Pan,[1]* Sun-Cheol Choi,[2]* He Wang,[3]* Yuanbo Qin,[3] Laura Volpicelli-Daley,[4]
Laura Swan,[4] Louise Lucast,[4] Cynthia Khoo,[5] Xiaowu Zhang,[6] Lin Li,[3] Charles S. Abrams,[5]
Sergei Y. Sokol,[2] Dianqing Wu[1]†

The canonical Wnt–β-catenin signaling pathway is initiated by inducing phosphorylation of one of the Wnt receptors, low-density lipoprotein receptor-related protein 6 (LRP6), at threonine residue 1479 (Thr[1479]) and serine residue 1490 (Ser[1490]). By screening a human kinase small interfering RNA library, we identified phosphatidylinositol 4-kinase type II α and phosphatidylinositol-4-phosphate 5-kinase type I (PIP5KI) as required for Wnt3a-induced LRP6 phosphorylation at Ser[1490] in mammalian cells and confirmed that these kinases are important for Wnt signaling in *Xenopus* embryos. Wnt3a stimulates the formation of phosphatidylinositol 4,5-bisphosphates [PtdIns (4,5)P$_2$] through frizzled and dishevelled, the latter of which directly interacted with and activated PIP5KI. In turn, PtdIns (4,5)P$_2$ regulated phosphorylation of LRP6 at Thr[1479] and Ser[1490]. Therefore, our study reveals a signaling mechanism for Wnt to regulate LRP6 phosphorylation.

Members of the Wnt family of secretory glycoproteins have important roles in various physiological and pathophysiological processes, including embryonic development, bone development, neuronogenesis, adipogenesis, myogenesis, organogenesis, lipid and glucose metabolism, and tumorigenesis (*1–5*). Canonical Wnt binds to two receptors, lipoprotein receptor-related protein 6 (LRP6) and frizzled (Fz) proteins, leading to phosphorylation of LRP6 at Thr[1479] by casein kinase Iγ and at Ser[1490] by glycogen synthase kinase 3 (GSK3) (*6–10*). Wnt appears to regulate Thr[1479] phosphorylation by inducing the formation of LRP6 aggregates (*9*), whereas it regulates Ser[1490] phosphorylation through GSK in an axin-dependent manner (*10*). To determine whether there are other kinases that take part in the regulation of LRP6 phosphorylation, we screened a human kinase small in-

[1]Department of Pharmacology, Yale University School of Medicine, New Haven, CT 06510, USA. [2]Department of Developmental and Regenerative Biology, Mount Sinai School of Medicine, New York, NY 10029, USA. [3]State Key Laboratory of Molecular Biology and Center of Cell Signaling, Institute of Biochemistry and Cell Biology, Shanghai Institutes for Biological Sciences, Chinese Academy of Sciences, Shanghai 200031, China. [4]Department of Cell Biology and Howard Hughes Medical Institute, Yale University School of Medicine, New Haven, CT 06510, USA. [5]Department of Medicine, University of Pennsylvania, Philadelphia, PA 19104, USA. [6]Cell Signaling Technology, Danvers, MA 01923, USA.

*These authors contribute equally to this work.
†To whom correspondence should be addressed. E-mail: dan.wu@yale.edu
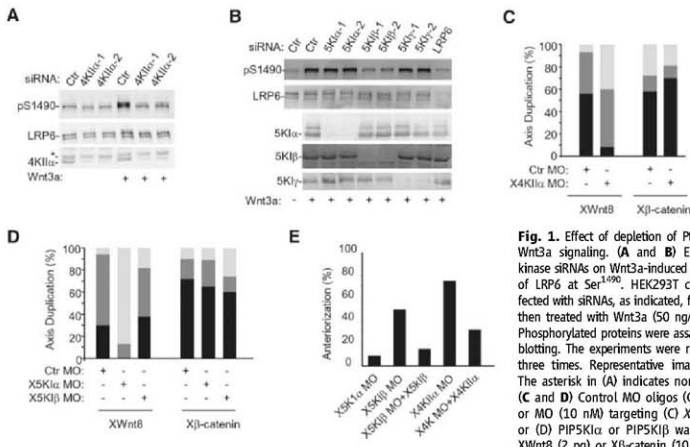

Fig. 1. Effect of depletion of PtdIns kinases on Wnt3a signaling. (**A** and **B**) Effects of PtdIns kinase siRNAs on Wnt3a-induced phosphorylation of LRP6 at Ser[1490]. HEK293T cells were transfected with siRNAs, as indicated, for 48 hours and then treated with Wnt3a (50 ng/ml) for 30 min. Phosphorylated proteins were assayed by Western blotting. The experiments were repeated at least three times. Representative images are shown. The asterisk in (A) indicates nonspecific bands. (**C** and **D**) Control MO oligos (Ctr MO, 10 nM) or MO (10 nM) targeting (C) *Xenopus* PI4KIIα or (D) PIP5KIα or PIP5KIβ was injected with XWnt8 (2 pg) or Xβ-catenin (10 pg) mRNA into four-cell stage embryos. *n* > 40 for all of the *Xenopus* embryo studies (where *n* is the number of examined embryos). Open bars, no double axis; light gray bars, incomplete double axis; black bars, complete double axis. (**E**) Four-cell stage embryos were injected with XPIP5KIβ MO (40 ng), XPI4KIIα MO (40 ng), or XPIP5KIα MO (40 ng) with or without XPIP5KIβ (10 pg) or XPI4KIIα (5 pg) RNA in the dorsal region and cultured to tailbud stages. XPIP5KIα MO, *n* = 30; XPIP5KIβ MO, *n* = 45; XPIP5KIβ MO+XPIP5KIβ, *n* = 29; XPI4KIIα MO, *n* = 55; and XPI4KIIα MO+XPI4KIIα, *n* = 30.

terfering RNA (siRNA) library from Applied Biosystems for effects on Wnt–induced accumulation of cytosolic β-catenin detected by an enzyme-linked immunosorbent assay (ELISA) and on phosphorylation of Ser[1490] of LRP6 detected by protein immunoblotting in human embryonic kidney (HEK) 293T cells (11). Multiple phosphatidylinositol (PtdIns) kinase siRNAs inhibited cytosolic β-catenin accumulation (fig. S1A and table S1) and the phosphorylation of LRP6 at Ser[1490] (Fig. 1, A and B) in response to purified Wnt3a protein. Among the tested PtdIns kinase siRNAs, siRNAs for phosphatidylinositol 4-kinase type II α (PI4KIIα) and phosphatidylinositol-4-phosphate 5-kinase type I β (PIP5KIβ) had the strongest inhibitory effects (Fig. 1, A and B, and fig. S1A). These siRNA also inhibited Wnt3a–induced reporter gene activity (fig. S1B). Additional siRNAs for both PI4KIIα and PIP5KIβ directed against different targeting sequences were also tested (Fig. 1, A and B, and fig. S1, B and C). To further verify that the effects of these siRNAs were specific, we restored Wnt signaling by expressing the kinases knocked down by the siRNAs (fig. S1, D to G). PI4KIIα and PIP5KIβ siRNAs did not inhibit lithium- and axin1/2 siRNA– induced accumulation of β-catenin, but β-catenin

siRNA did (fig. S1, C and H). Thus, these siRNAs appeared to affect Wnt signaling by affecting LRP6 phosphorylation rather than Wnt signaling downstream components.

PIP5KIγ siRNAs also showed a weak inhibitory effect, whereas PIP5KIα siRNAs had no effect in HEK293T cells (Fig. 1B). However, treatment of the cells with combinations of the PIP5KI siRNAs showed that the combination targeting all three PIP5KI isoforms reduced Wnt3a-induced accumulation of β-catenin and phosphorylation of LRP6 almost to basal levels (fig. S1, C and I), suggesting that PIP5KIα and Iγ may also contribute to Wnt signaling in these cells.

We next examined the roles of the PtdIns kinases in Wnt signaling with the use of Xenopus embryos. A morpholino (MO) targeting Xenopus PI4KIIα inhibited XWnt8-induced, but not β-catenin–induced, axis duplication in Xenopus embryos (Fig. 1C and fig. S2A). Although PIP5KIβ MO showed little effect, a MO targeting its close homolog PIP5KIα inhibited XWnt8-induced, but not β-catenin–induced, axis duplication (Fig. 1D). Consistent with the phenotypes, PIP5KIα and PI4KIIα MOs reduced phosphorylation of LRP6 (fig. S2B). In addition, the expression of catalyt-

ically inactive PIP5KIα and PI4KIIα mutants suppressed axial duplication induced by XWnt8, but not by β-catenin (fig. S2C), further confirming the importance of these kinases in Wnt signaling.

Inhibition of zygotic Wnt–β-catenin signaling induces anteriorized phenotypes that include enlarged cement glands and head structures (12). PI4KIIα MO that was injected into the dorsal regions of Xenopus embryos induced strong anteriorized phenotypes in more than 70% of embryos. This effect could be partially reversed by coinjection of Xenopus PI4KIIα mRNA (Fig. 1E and fig. S2D). Although PIP5KIα MO had little effect on the phenotype, PIP5KIβ MO induced anteriorized phenotypes in ~50% of the treated embryos. The PIP5KIβ MO effect could be almost completely reversed by the injection of XPIP5KIβ mRNA (Fig. 1E and fig. S2D). Together, these results indicate that PtdIns kinases regulate endogenous Wnt signaling in Xenopus embryos.

Because sequential phosphorylation of PtdIns lipids by PI4KII and PIP5KI constitutes the major pathway for PtdIns $(4,5)P_2$ production in most cells (13, 14), we suspected that PtdIns $(4,5)P_2$ might regulate the phosphorylation of LRP6 at Ser[1490]. To test this hypothesis, we delivered PtdIns, plus all of the seven possible isoforms of PtdIns phosphates at equal molar concentrations, into HEK 293T cells in a lipid carrier. PtdIns $(4,5)P_2$ showed the strongest stimulatory effect on Wnt3a-induced phosphorylation of Ser[1490] (Fig. 2A). In addition, the delivery of PtdIns (4)P (but not PtdIns) rescued the effect of PI4K siRNA, whereas the delivery of PtdIns $(4,5)P_2$ (but not PtdIns (4)P) rescued the effect of PIP5K siRNA on Wnt3a-induced phosphorylation of LRP6 (Fig. 2, B and C) and β-catenin accumulation (fig. S3). These results suggest that PtdIns $(4,5)P_2$ may be the primary PtdIns lipid involved in the regulation of Ser[1490] phosphorylation.

We used a rapidly inducible PtdIns $(4,5)P_2$ hydrolysis system to further investigate the role of PtdIns $(4,5)P_2$ in regulating phosphorylation of LRP6. In this system, rapamycin induces the heterodimerization of membrane-targeted FRP (fragment of mammalian target of rapamycin that binds FKBP12) and FKBP12 (FK560–binding protein 12) fused with a truncated form of type IV phosphoinositide 5-phosphatase, leading to activation of the phosphatase (15, 16). As shown in Fig. 2D, rapamycin reduced the amount of PtdIns $(4,5)P_2$ in cells expressing both FRP and phosphatase-fused FKBP12, but not in those expressing FRP and FKBP12 alone. Rapamycin also attenuated phosphorylation of LRP6 only in cells expressing both FRP and phosphatase-fused FKBP12 (Fig. 2E).

To determine whether Wnt3a can stimulate PtdIns $(4,5)P_2$ production, we established a PtdIns $(4,5)P_2$ ELISA and detected significant Wnt3a-induced formation of PtdIns $(4,5)P_2$ (more than twofold increases) in HEK293T, Hela, and NIH3T3 cells (fig. S4A). We confirmed these results by high-performance liquid chromatography (HPLC) and thin-layer chromatography (TLC) (Fig. 3A and fig. S4, B and C). Together with the findings that the PI4KIIα siRNA abolished (and the PIP5KIβ siRNA
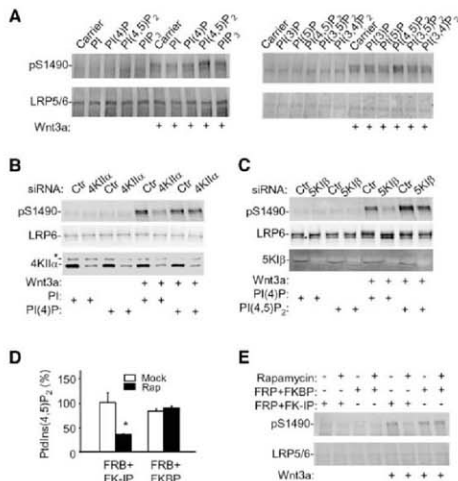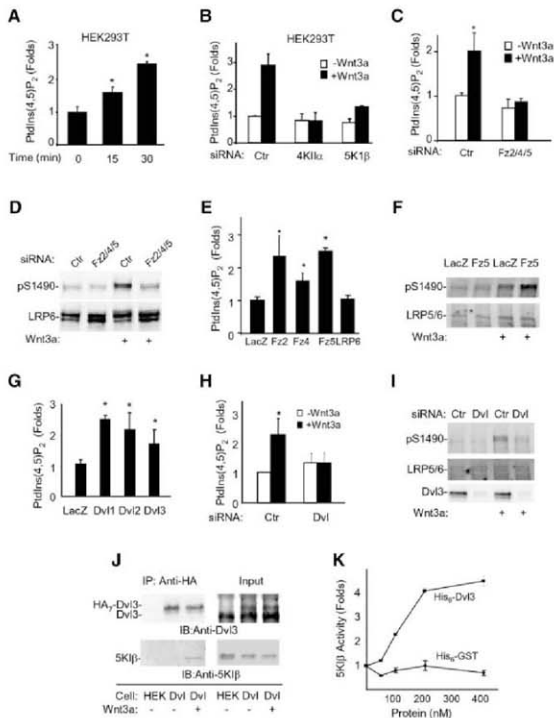

Fig. 2. Effect of PtdIns $(4,5)P_2$ on Wnt3a signaling. (**A**) Effect of exogenous PtdIns $(4,5)P_2$ on Wnt3a-induced phosphorylation of LRP6 at Ser[1490]. HEK293T cells were treated with various PtdIns lipids in a lipid carrier for 10 min and incubated with Wnt3a (20 ng/ml) for an additional 20 min before being assayed by immunoblotting. (**B** and **C**) Rescuing the effects of PI kinase siRNAs by direct delivery of PtdIns lipids. The asterisk in (B) indicates nonspecific bands. (**D** and **E**) Reduction in PtdIns $(4,5)P_2$ levels decreases LRP6 Ser[1490] phosphorylation. HEK293T cells transfected with FRB (PM-FRB-CFP), FKBP (mRFP-FKBP12), or FK-IP (mRFP-FKBP12-5-ptase-dom) were treated with Wnt3a (20 ng/ml) in the presence or absence of rapamycin (100 nM) for 30 min before they were collected for the lipid assay (D) and immunoblotting analysis (E). *P < 0.01 compared with the same transfection in the absence of rapamycin (Student's t test). Error bars indicate SDs.

Fig. 3. Stimulation of PtdIns $(4,5)P_2$ formation by Wnt3a through Fz and DVl. (**A**) Effect of Wnt3a treatment on PtdIns $(4,5)P_2$ content. HEK293T Cells were stimulated with Wnt3a protein (50 ng/ml) before lipid extraction. PtdIns $(4,5)P_2$ content was determined by HPLC. *$P < 0.01$ compared with time 0 (Student's t test). (**B**) Requirement of PI4KIIIα and PIP5KIβ for Wnt3a-induced formation of PtdIns $(4,5)P_2$. Cells were transfected with siRNAs, as indicated, for 48 hours and then treated with Wnt3a (50 ng/ml) for 30 min. PtdIns $(4,5)P_2$ were detected by ELISA. (**C**) Effect of Fz siRNAs on Wnt3a-induced formation of PtdIns $(4,5)P_2$. Cells were transfected with control siRNA or a combination of Fz2, Fz4, and Fz5 siRNAs for 48 hours and then treated with Wnt3a (50 ng/ml) for 30 min before assays. *$P < 0.01$ compared with control siRNA transfection in the absence of Wnt3a (Student's t test). (**D**) Effect of Fz siRNAs on Wnt3a-induced phosphorylation of LRP6 at Ser^{1490}. Cells were transfected as in (C) and then treated with Wnt3a (50 ng/ml) for 30 min. (**E**) Effect of Fz overexpression on accumulation of PtdIns $(4,5)P_2$. HEK293T cells were transfected with the LacZ, Fz5, or LRP6 expression plasmids for 18 hours, and PtdIns $(4,5)P_2$ levels were determined by ELISA. *$P < 0.01$ compared with the sample expressing LacZ (Student's t test). (**F**) Effect of Fz5 expression on phosphorylation of LRP6 at Ser^{1490}. Cells were transfected with Fz5 expression plasmid for 18 hours and then treated with Wnt3a (20 ng/ml) for 20 min. (**G**) Effect of DVl expression on the PtdIns $(4,5)P_2$ levels. HEK293T cells were transfected with the mouse DVl1, 2, or 3 expression plasmid for 18 hours before the PtdIns $(4,5)P_2$ ELISA assay. *$P < 0.01$ compared with the sample expressing LacZ (Student's t test). (**H** and **I**) Effect of DVl siRNAs on formation of PtdIns $(4,5)P_2$ and phosphorylation of LRP6 at Ser^{1490}. HEK293T cells were transfected with control siRNA or DVl siRNA mixture targeting DVl1, 2, and 3 for 48 hours and then treated with Wnt3a (50 ng/ml) for 30 min. *$P < 0.01$ compared with control siRNA transfection in the absence of Wnt3a (Student's t test). (**J**) Interaction of DVl3 with endogenous PIP5KIβ. HEK293T cells (DVl) stably expressing DVl3-HA$_7$ were used in immunoprecipitation by an antibody against HA (anti-HA). The parent HEK293T cells (HEK) were used as a control. Immuno-complexes were detected by the anti-DVl3 and anti-PIP5KIβ antibodies. (**K**) Effect of purified recombinant DVl3 protein on kinase activity of purified recombinant PIP5KIβ protein. PIP5KIβ (50 nM) was incubated with the GST (glutathione S-transferase)or DVl3 proteins for 2 hours at room temperature. One-tenth of the samples was taken for Western blotting, and the rest was subjected to in vitro kinase assay with PtdIns (4)P as a substrate. The product PtdIns $(4,5)P_2$ is separated by TLC, detected, and quantified by a phosphoimager. Error bars indicate SDs in all panels.
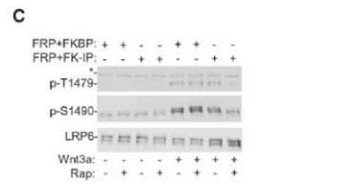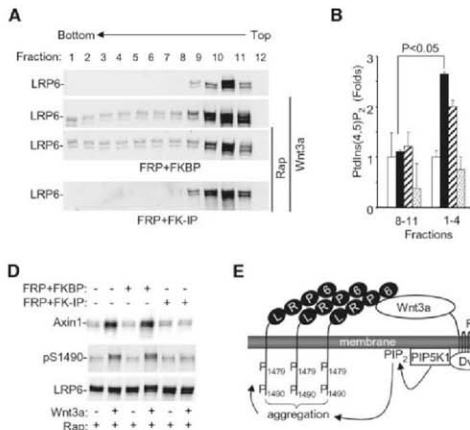
reduced) Wnt3a-induced accumulation of PtdIns $(4,5)P_2$ (Fig. 3B), we conclude that Wnt3a stimulates PtdIns $(4,5)P_2$ production via these PtdIns kinases.

We next investigated whether Fz is required for Wnt3a-induced formation of PtdIns $(4,5)P_2$ and detected expression of Fz2, 3, 4, 5, and 6 in HEK293T cells by reverse transcription polymerase chain reaction (table S2). We made and validated two sets of siRNAs for each of these Fz genes (table S2). Fz5 siRNA showed the strongest inhibition of Wnt3a-induced accumulation of β-catenin, whereas Fz2 and Fz4 siRNAs also had some inhibitory effect (fig. S5B and table S2). The combination of Fz2, 4, and 5 siRNAs virtually abolished Wnt3a-induced accumulation of β-catenin (table S2). This combination also abrogated Wnt3a-induced forma-tion of PtdIns $(4,5)P_2$ (Fig. 3C) and phosphoryl-ation of LRP6 at Ser^{1490} (Fig. 3D, fig. S5C, and table S2). On the other hand, expression of Fz5, 2, and 4 stimulated the formation of PtdIns $(4,5)P_2$ (Fig. 3E) and Wnt3a-induced phosphorylation of Ser^{1490} (Fig. 3F, figs. S5, D and E). These results together indicate that Wnt3a acts through Fz to stimulate PtdIns $(4,5)P_2$ formation in HEK293T cells and regulates LRP6 phosphorylation.

Because dishevelled (DVl) is required for the phosphorylation of LRP6 (9, 10), we questioned whether DVl might have a role in the formation of PtdIns $(4,5)P_2$. Expression of DVl1-3 increased the amount of PtdIns $(4,5)P_2$ in HEK293T cells (Fig. 3G and fig. S6A). When HEK293T cells were transfected with a mixture of three DVl siRNAs tar-geting each of the three DVl isoforms (17), both Wnt3a-induced formation of PtdIns $(4,5)P_2$ and phosphorylation of Ser^{1490} were inhibited (Fig. 3, H and I, and fig. S6B). DVl is a scaffold protein with no known enzymatic domains. We tested whether DVl and PIP5KIβ interacted and found that they coimmunoprecipitated when overexpressed in HEK293T cells (fig. S6C). We mapped DVl interac-tion site to the N-terminal half of PIP5KIβ kinase domain (fig. S6D) and PIP5KI-binding sites to two fragments of DVl that contain the DIX and PDZ domains, respectively (fig. S6E). The interaction of DVl3 and PIP5KIβ was also examined in a HEK293T cell line that stably expressed DVl3 car-rying seven hemagglutinin (HA) tags at its C ter-minus at a level lower than that of endogenous DVl3

Fig. 4. Requirement of PtdIns $(4,5)P_2$ for formation of LRP6 aggregate and membrane translocation of axin and GSK3. (**A**) Requirement of PtdIns $(4,5)P_2$ for Wnt3a-induced LRP6 aggregation. HEK293T cells were transfected and treated with Wnt3a and rapamycin as indicated. Cell lysates were subjected to sucrose density-gradient ultracentrifugation, and fractions were analyzed by Western analysis. (**B**) PtdIns $(4,5)P_2$ content in two sucrose density-gradient ultracentrifugation fraction pools. Fractions 8 to 11 and 1 to 4 from (A) were pooled, and PtdIns $(4,5)P_2$ amounts were measured by ELISA. Open bars correspond to the samples from the top panel in (A); black bars to the second panel; striped bars to the third panel; and dotted bars to the last panel. The PtdIns $(4,5)P_2$ amounts are presented relative to those in untreated cells. Error bars indicate SDs. (**C**) Requirement of PtdIns $(4,5)P_2$ for phosphorylation of LRP6 at Thr[1479]. HEK293T cells were transfected with plasmids, as indicated, for 20 hours and then treated with Wnt3a (20 ng/ml) for 30 min in the presence or absence of rapamycin (100 nM) before they were collected for immunoblotting analysis. The asterisk indicates nonspecific bands. (**D**) Requirement of PtdIns $(4,5)P_2$ for Wnt3a-induced membrane recruitment of axin1. HEK293T cells were transfected and treated as indicated. The membrane fractions were prepared and analyzed by Western analysis. (**E**) Model for Wnt3a cross-membrane signaling.

(upper right panel in Fig. 3J). Although we did not observe coimmunoprecipitation in the absence of Wnt3a, an interaction of Dvl3-HA with endogenous PIP5KIβ was detected in the presence of Wnt3a (Fig. 3J), suggesting that Wnt3a may regulate the interaction. In a pull-down assay with recombinant proteins prepared in *E. coli*, Dvl1 interacted with PIP5KIβ and Iα in vitro (fig. S6F). We then tested whether Dvl could directly regulate PIP5KI kinase activity. Using the recombinant Dvl3 and PIP5KIβ prepared from *E. coli*, we found that, in an in vitro kinase assay, Dvl directly stimulated PIP5KIβ in a dose-dependent manner (Fig. 3K and fig. S6G). Together with the knowledge that Dvl interact with Dvl and recruit it to the membranes (9, 18–23), the above data suggest that Wnt3a may induce (through Fz) Dvl to bind and activate PIP5KI.

We next tested whether PtdIns $(4,5)P_2$ is required for Wnt3a-induced formation of LRP6 aggregates (referred to as "signalosomes"), which precedes phosphorylation of LRP6 at Thr[1479] (9). We used sucrose density-gradient centrifugation to detect LRP6 aggregates (Fig. 4A). Fractions that contained LRP6 aggregates also had a higher PtdIns $(4,5)P_2$ content than did fractions containing nonaggregated LRP6 (Fig. 4B). Notably, the aggregation was sensitive to the elimination of PtdIns $(4,5)P_2$ through rapamycin-induced PtdIns $(4,5)P_2$ hydrolysis (Fig. 4A). We also examined LRP6 aggregation using confocal microscopy in Hela cells expressing LRP6-YFP (9). We observed the aggregates in control cells but not in cells transfected with the PIP5KI siRNAs (fig. S7). Elimination of PtdIns $(4,5)P_2$ also led to decreased phosphorylation of

Thr[1479] (Fig. 4C) (9). Therefore, we conclude that PtdIns $(4,5)P_2$ is required for Wnt-induced LRP6 aggregation and Thr[1479] phosphorylation.

Because LRP6 aggregates appear to have a high affinity for axin (9) and because axin membrane translocation is required for GSK3-mediated phosphorylation of Ser[1490] (10), we examined if PtdIns $(4,5)P_2$ is involved in Wnt-induced axin membrane translocation. Elimination of PtdIns $(4,5)P_2$ using the rapamycin-inducible PtdIns $(4,5)P_2$ hydrolysis system abrogated Wnt3a-induced axin translocation (Fig. 4D). Putting all of these results together, we propose a model (Fig. 4E) to suggest that Wnt3a regulates the activity of PIP5KI through Fz and Dvl and induces the formation of PtdIns $(4,5)P_2$. PtdIns $(4,5)P_2$ is required, but not sufficient, for LRP6 aggregation and phosphorylation at both Thr[1479] and Ser[1490], as well as for axin translocation. Precise mechanisms by which PtdIns $(4,5)P_2$ regulates these Wnt signaling events, however, need to be investigated further.

References and Notes

1. C. Y. Logan, R. Nusse, *Annu. Rev. Cell Dev. Biol.* **20**, 781 (2004).
2. T. Reya, H. Clevers, *Nature* **434**, 843 (2005).
3. H. Clevers, *Cell* **127**, 469 (2006).
4. R. T. Moon, A. D. Kohn, G. V. De Ferrari, A. Kaykas, *Nat. Rev. Genet.* **5**, 691 (2004).
5. A. Mani et al., *Science* **315**, 1278 (2007).
6. G. Davidson et al., *Nature* **438**, 867 (2005).
7. R. Nusse, *Nature* **438**, 747 (2005).
8. X. Zeng et al., *Nature* **438**, 873 (2005).
9. J. Bilić et al., *Science* **316**, 1619 (2007).
10. X. Zeng et al., *Development* **135**, 367 (2007).
11. Materials and methods are available as supporting material on *Science* Online.
12. R. Harland, J. Gerhart, *Annu. Rev. Cell Dev. Biol.* **13**, 611 (1997).
13. J. J. Hsuan, S. Minogue, M. dos Santos, *Adv. Cancer Res.* **74**, 167 (1998).
14. R. L. Doughman, A. J. Firestone, R. A. Anderson, *J. Membr. Biol.* **194**, 77 (2003).
15. D. W. Heo et al., *Science* **314**, 1458 (2006), published online 8 November 2006; 10.1126/science.1134389.
16. P. Varnai, B. Thyagarajan, T. Rohacs, T. Balla, *J. Cell Biol.* **175**, 377 (2006).
17. L. Li, J. Mao, L. Sun, W. Liu, D. Wu, *J. Biol. Chem.* **277**, 5977 (2002).
18. J. D. Axelrod, J. R. Miller, J. M. Shulman, R. T. Moon, N. Perrimon, *Genes Dev.* **12**, 2610 (1998).
19. H. C. Wong et al., *Mol. Cell* **12**, 1251 (2003).
20. W. Chen et al., *Science* **301**, 1391 (2003).
21. F. Cong, L. Schweizer, H. Varmus, *Development* **131**, 5103 (2004).
22. W. J. Pan et al., *Cell Res.* **14**, 324 (2004).
23. N. Yokoyama, D. Yin, C. C. Malbon, *J. Mol. Signal.* **2**, 11 (2007).
24. We thank P. De Camilli for making available resources from his lab in connection to this work, discussion, and critical reading of the manuscript; Z. Li, M. Orsulak, Y. Zhang, L. Tang, W. Liu, Y. Xi, F. Nie, Y. Wu, and X. Gan for technical assistance; and D. Sussman, C. Carpenter, R. Grosschedl, T. Balla, B. Williams, M. F. Roussel, X. He, C. Niehrs, R. Nusse, and J. Nathans for providing experimental materials. This work was supported by grants from NIH (AR051476, CA132317, HL080706, NS36251, and DA018343), the National Institute on Drug Abuse to Yale Neuroproteomics Center, the Ministry of Science and Technology of China (2002CB513000), and the National Science Foundation of China (30521005).

Helical Structures of ESCRT-III Are Disassembled by VPS4

Suman Lata,[1] Guy Schoehn,[1,2] Ankur Jain,[3]* Ricardo Pires,[1] Jacob Piehler,[3] Heinrich G. Göttlinger,[4] Winfried Weissenhorn[1]†

During intracellular membrane trafficking and remodeling, protein complexes known as the ESCRTs (endosomal sorting complexes required for transport) interact with membranes and are required for budding processes directed away from the cytosol, including the budding of intralumenal vesicles to form multivesicular bodies; for the budding of some enveloped viruses; and for daughter cell scission in cytokinesis. We found that the ESCRT-III proteins CHMP2A and CHMP3 (charged multivesicular body proteins 2A and 3) could assemble in vitro into helical tubular structures that expose their membrane interaction sites on the outside of the tubule, whereas the AAA-type adenosine triphosphatase VPS4 could bind on the inside of the tubule and disassemble the tubes upon adenosine triphosphate hydrolysis. CHMP2A and CHMP3 copolymerized in solution, and their membrane targeting was cooperatively enhanced on planar lipid bilayers. Such helical CHMP structures could thus assemble within the neck of an inwardly budding vesicle, catalyzing late steps in budding under the control of VPS4.

ESCRT (endosomal sorting complexes required for transport) complexes 0, I, II, and III and accessory proteins regulate cell surface receptor sorting into intralumenal endosomal vesicles, generating multivesicular bodies (MVBs) (1–3). ESCRTs are also recruited during budding of some enveloped viruses (4) and cytokinesis (5, 6), processes that are topologically similar to vesicle budding into endosomes.

Yeast expresses six ESCRT-III–like proteins (7), whereas mammalian cells express 10, known as charged multivesicular body protein (CHMP) 1 to 6 (8). C-terminally truncated CHMP3 has a four helical bundle core and two regions that are important for CHMP polymerization and membrane targeting (9). CHMPs exist in an auto-inhibited state in the cytosol (10, 11); removal of autoinhibition induces membrane targeting (9, 12, 13) and ESCRT-III assembly into a putative protein lattice (1, 2). Overexpression of SNF7/CHMP4 in mammalian cells produces filaments that induce outward buds in the presence of catalytically inactive VPS4 (14), but little is known about heteromeric polymerization by ESCRT-III proteins.

The recruitment of the AAA-type adenosine triphosphatase (ATPase) VPS4 is essential for the termination of the budding process and catalyzes disassembly of the complex (2, 15, 16). The central role of ESCRT-III and VPS4 in all known ESCRT-catalyzed budding events is further underlined by the inhibitory effects of dominant negative mutants of ESCRT-III (8, 9, 17, 18) and VPS4 (2, 5, 18) on MVB formation, HIV-1 budding, and cytokinesis.

Yeast Vps2p (CHMP2) and Vps24p (CHMP3) form a subcomplex (7) consistent with the heterodimerization potential suggested by the CHMP3 crystal structure (9). Such subcomplexes may thus represent the building blocks for polymerization. We set out to study the interactions and polymerization mode of CHMP2 and CHMP3 in vitro. Interactions between full-length autoinhibited CHMP3 and CHMP2A could not be detected, and so both proteins were produced as C-terminal truncations (fig. S1A; CHMP2AΔC and CHMP3ΔC) in their proposed activated forms (9, 10, 13). Whereas CHMP3ΔC was monodisperse in solution (9), CHMP2AΔC fused to the maltose binding protein (MBP) formed monomers and concentration-dependent aggregates (fig. S1B). Co-incubation of monomeric CHMP2AΔC and CHMP3ΔC led to the formation of oligomers, migrating to the bottom fraction of a sucrose gradient (Fig. 1A). CHMP2AΔC and CHMP3ΔC assembled into long tubular structures (Fig. 1B), with the majority of the particles revealing a di-

[1]Unit for Virus Host Cell Interaction, UMR 5233 UJF (Université Joseph Fourier)-EMBL (European Molecular Biology Laboratory)-CNRS, 6 rue Jules Horowitz, 38042 Grenoble Cedex 9, France. [2]Institut de Biologie Structurale UMR 5075 CEA (Commissariat à l'Énergie Atomique)-CNRS-UJF, 41 rue Jules Horowitz, 38027 Grenoble Cedex 1, France. [3]Institute of Biochemistry, Johann Wolfgang Goethe University, Max-von-Laue Straße 9, 60438 Frankfurt am Main, Germany. [4]Program in Gene Function and Expression, Program in Molecular Medicine, University of Massachusetts Medical School, Worcester, MA 01605, USA.

*Present address: Department of Physics, University of Illinois at Urbana-Champaign, 1110 West Green Street, Urbana, IL 61801–3080, USA.
†To whom correspondence should be addressed. E-mail: weissenhorn@embl.fr
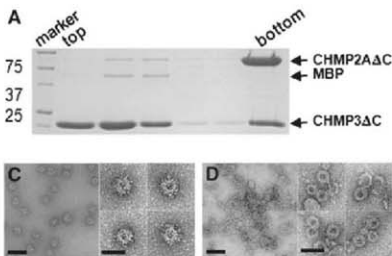
Fig. 1. CHMP2AΔC-CHMP3ΔC polymer formation. (**A**) Sucrose density gradient analysis of CHMP2AΔC-CHMP3ΔC complex formation. (**B**) Negative staining EM of tubular structures formed by CHMP2AΔC and CHMP3ΔC. Negative staining EM (**C**) of CHMP2AΔC and (**D**) of CHMP2AΔC after removal of MBP. Scale bars indicate 100 nm; inset scale bars, 50 nm.
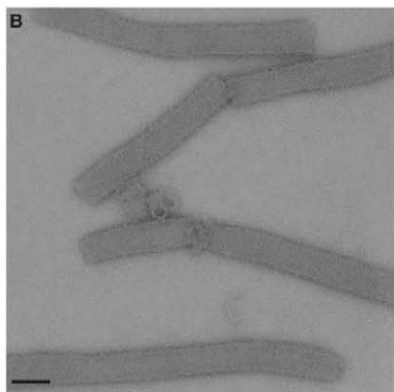
Fig. 2. Cryo EM of CHMP2AΔC-CHMP3ΔC (**A**) tubes and (**B**) tubes after removal of MBP from CHMP2AΔC. Scale bars, 100 nm. (**C**) The EM reconstruction model showing the 45 Å width of the helical structure produced by the CHMP lattice (top view).
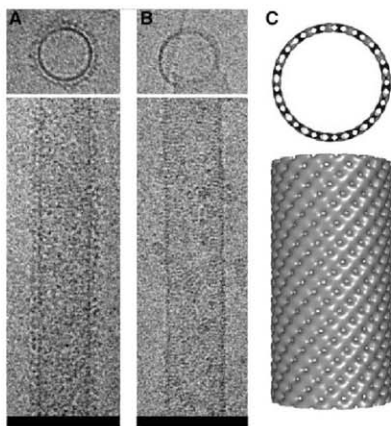

Fig. 3. CHMP2AΔC-CHMP3 tube disassembly by VPS4B. (**A**) Negative staining EM of tubes formed by CHMP2AΔC and CHMP3. Sucrose gradient analysis of (**B**) CHMP2AΔC, (**C**) CHMP3, (**D**) VPS4B, (**E**) CHMP2AΔC-CHMP3-VPS4B complex formation, and (**F**) CHMP2AΔC-CHMP3-VPS4B complexes after incubation with ATP Mg²⁺. (**G**) Negative staining EM of CHMP2AΔC-CHMP3 tubes revealing VPS4B on the inside. Radial density profile (**H**) of a CHMP2AΔC-CHMP3-VPS4B and (**I**) of CHMP2AΔC-CHMP3 tubes calculated across the cross section of the tube. (**J**) Negative staining EM after adding ATP Mg²⁺ to CHMP2AΔC-CHMP3-VPS4B tubes. (**K**) Disassembly of fluorescein-labeled CHMP2AΔC-CHMP3 tubes measured by change in emission intensity upon addition of HBS (magenta), 10 μM VPS4B (blue), 10 μM VPS4B plus 100 μM AMP-PNP Mg²⁺ (green), 5 μM VPS4B plus 50 μM ATP Mg²⁺ (black), and 10 μM VPS4B plus 100 μM ATP Mg²⁺ (red). (Inset) The fluorescein-labeled CHMP2AΔC and CHMP3 visualized on an SDS–polyacrylamide gel. Scale bars, 100 nm.
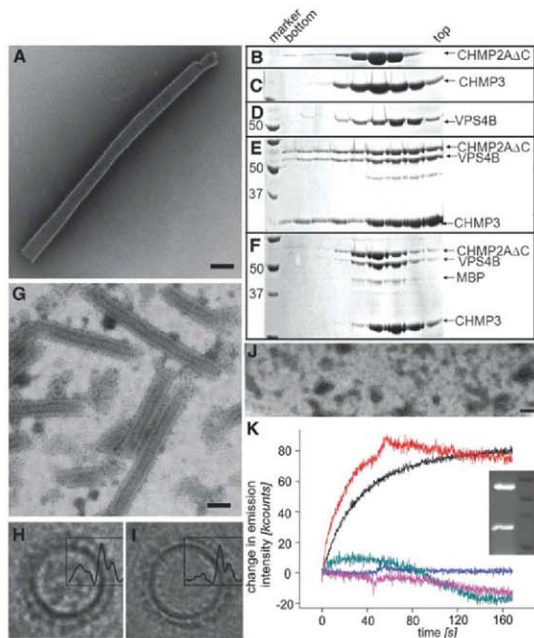
ameter of ~40 nm and a small fraction showing deviations up to 70 nm in negative staining electron microscopy (EM).

Although neither CHMP3, CHMP3ΔC, nor CHMP2A formed higher-order oligomers on their own, CHMP2AΔC sedimented in a sucrose gradient (fig. S1C) and formed ringlike structures (Fig. 1C). Removal of MBP produced particles with inner and outer diameters of ~12 nm and ~30 nm, respectively. Increased aggregation upon MBP cleavage and the exclusive face-up orientations (Fig. 1D) hindered determination of the ring thickness.

Cryo-EM of the CHMP2AΔC-CHMP3ΔC polymer showed tubes with a fuzzy surface (Fig. 2A). Removal of MBP from CHMP2AΔC rendered the surface smooth, revealing striations perpendicular to the longitudinal axis of the tube

(Fig. 2B). Because image analyses of MBP-cleaved tubes was hindered by their aggregation, we applied the iterative helical real space reconstruction algorithm (19) to reconstruct volumes from the tubes containing MBP attached to CHMP2AΔC (20). The 32 Å pitch of the helical assembly was determined by the Fourier transform of the images (20). The calculated helical structure contains 16.57 repeating units per turn, with inner and outer diameters of 43 nm and 52 nm, respectively (Fig. 2C). The CHMP2A-CHMP3 dimer model could fit into the repeating unit of the EM map (20) (fig. S2, A to D), exposing the membrane targeting surface to the outside and the VPS4B interaction site toward the inside of the tube (fig. S2, D and E).

The organization of the CHMP2AΔC-CHMP3ΔC polymer did not indicate how other CHMPs could participate in the same polymer.

In fact, monomeric CHMP4BΔC did not integrate into CHMP2AΔC-CHMP3ΔC tubes (fig. S3) despite similarities in polymerization (14). Although CHMP4 may participate in CHMP2A-CHMP3 tube formation as a CHMP4-CHMP6 subcomplex (7), different ESCRT-III complexes may be formed in vivo that interact (7) and act sequentially.

Because the VPS4B-CHMP interaction requires an intact C terminus (21, 22), we used full-length proteins for tube formation. Whereas CHMP2AΔC and CHMP3 formed similar tubes to those formed with CHMP3ΔC (Figs. 1B and 3A), combinations of CHMP2A and CHMP3 and CHMP2A and CHMP3ΔC did not polymerize. In sucrose gradient centrifugation, isolated forms of CHMP2AΔC, CHMP3, and VPS4B floated at similar positions (Fig. 3, B and C), consistent with monomeric or dimeric VPS4B in the absence of adenosine triphosphate (ATP) (23). Mixing all three proteins recruited them to the pellet fraction, corroborating the CHMP3-VPS4B interaction (Fig. 3E). Negative staining EM of the CHMP2AΔC-CHMP3 tubes assembled in the presence of VPS4B revealed additional electron-dense material along the longitudinal axis of the tubes (Fig. 3G). Radial density profiles of cross sections obtained by cryo-EM (fig. S4B) showed a broad central peak, confirming the VPS4B presence inside the tubes, followed by a sharp peak corresponding to the CHMP lattice and a smaller peak corresponding to MBP attached to CHMP2AΔC (Fig. 3H and fig. S4D). In contrast, in cross sections of tubes without VPS4B (fig. S4A), the central peak of the density profile did not rise above the background signal (Fig. 3I and fig. S4C). Thus, VPS4B used CHMP2AΔC-CHMP3 tubes as a scaffold for assembly, which apparently produced disordered VPS4B oligomers in the absence of ATP. Addition of ATP and Mg^{2+} to the CHMP2AΔC-CHMP3-VPS4B tubular structures induced disassembly of the tubes (Fig. 3, F and J). Incubation of fluorescein-labeled tubes (fig. S5) with buffer, VPS4B, or VPS4B plus adenylyl-imidodiphosphate (AMP-PNP) Mg^{2+} showed no change in emission intensity as a function of time (Fig. 3K). In contrast, dequenching, indicating disassembly, was measured as an increase in emission intensity when the tubes were incubated with VPS4B plus ATP Mg^{2+} (Fig. 3K). Thus, VPS4B induced tube disassembly in vitro.

CHMPs are selectively targeted to cellular membranes (7, 13, 24), which requires an extended basic surface in case of CHMP3 (9). With reflectometric interference spectroscopy (RIfS) (20), CHMP2AΔC, CHMP3ΔC, and their complex showed no notable mass deposition (<0.10 ng mm^{-2}) on silica-supported bilayers composed of 1-stearoyl-2-oleoyl-sn-glycero-3-phosphocholine (SOPC) lipids (Fig. 4A). However, CHMP3ΔC bound to 1,2-dioleoyl-sn-glycero-3-phosphoserine (DOPS):SOPC bilayers (fig. S6) with an equilibrium binding amplitude (Γ_{eq}) of 1.08 ng mm^{-2} and dissociated with a rate of (k_d) ~ 0.3 s^{-1}, whereas CHMP2AΔC (4 μM) showed a Γ_{eq} of
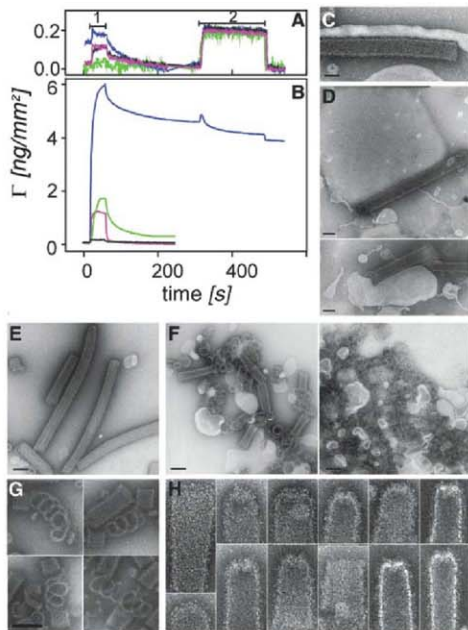

Fig. 4. CHMP protein membrane interaction. (**A**) Binding curves measured by RIfS on a SOPC bilayer: MBP (black), CHMP3ΔC (magenta), CHMP2AΔC (green), and CHMP2AΔC-CHMP3ΔC (blue). (**B**) Binding curves measured by RIfS on a DOPS:SOPC bilayer: MBP (black), CHMP3ΔC (magenta), CHMP2AΔC (green), and CHMP2AΔC-CHMP3ΔC (blue). Protein injections were followed by injection of 1 M NaCl in HBS. CHMP2AΔC-CHMP3ΔC tubes (**C**) with and (**D**) without MBP attached to CHMP2AΔC. (**E**) CHMP2AΔC-CHMP3ΔC tubes assembled in the presence of SOPC LUVs. (**F**) CHMP2AΔC-CHMP3ΔC tubes assembled in the presence of 0.5 mg ml^{-1} (left) and 1.5 mg ml^{-1} (right). SOPC:DOPS LUVs are shorter, (**G**) reveal single helical coils, and (**H**) are often cone-shaped. Scale bars, 100 nm.